

Estimation of Intraoperative Brain Deformation

Songbai Ji, Xiaoyao Fan, Alex Hartov, David W. Roberts and Keith D. Paulsen

Abstract Image-guided neuronavigation based on preoperative images has become the standard-of-care in many open cranial surgeries. The accuracy of patient registration between structures of interest in the operating room and pre-operative images is essential for effective deployment of image-guidance. Brain shift is widely recognized as the single most important factor that degrades registration accuracy during surgery. Intraoperative imaging techniques are important to compensate for brain shift. However, they alone are either impractical for broad clinical acceptance due to high capital cost and intrusion on surgical workflow (e.g., intraoperative magnetic resonance) or insufficient to provide full-field image data for neuronavigation (e.g., intraoperative ultrasound, stereovision, and laser range scanning). Alternatively, biomechanical models are becoming increasingly attractive for estimating brain deformation intraoperatively because they offer whole-brain displacement fields from which to generate model-updated MR images for subsequent guidance, and are low in cost. Because parenchymal feature displacements derived from intraoperative images can be incorporated into model computation, brain deformation is estimated on a patient-specific basis and may allow sufficient accuracy in image-to-patient registration to be maintained throughout surgery. Apparently, the clinical feasibility of this technique for application in the OR depends on the performance of the modeling updates as well as the generation of feature displacements from intraoperative images. This

S. Ji (✉) · X. Fan · A. Hartov · K. D. Paulsen
Thayer School of Engineering, Dartmouth College,
14 Engineering Drive, Hanover, NH 03755, USA
e-mail: Songbai.Ji@Dartmouth.EDU

A. Hartov · D. W. Roberts · K. D. Paulsen
Norris Cotton Cancer Center, Lebanon, NH 03756, USA

D. W. Roberts
Dartmouth Hitchcock Medical Center, Lebanon, NH 03756, USA

chapter presents details on the important aspects of a computational scheme for estimating intraoperative whole-brain deformation to produce an updated MR image volume. Preliminary results using intraoperative fluorescence imaging for validation of model estimation are also described.

1 Introduction

Computer-assisted neuronavigation based on preoperative images has become the standard-of-care in many open cranial procedures because it allows effective and more efficient operations to occur in the brain with less invasiveness. Once the patient's head is registered in the operating room (OR) with preoperative images (most often, preoperative magnetic resonance images, or pMR) to establish a one-to-one spatial transformation between anatomy in physical space and the corresponding image space, localization of tissue of interest (e.g., tumor) can then be achieved by navigating through the preoperative scans. Successful application of this image-guidance technology has proved to be essential for brain tumor resection where it has become increasingly evident that surgical accuracy is critical to patient prognosis [1–3]. For example, a recent analysis of 416 patients with glioblastoma multiforme found that resection of 89% of the tumor volume was necessary to improve patient survival while resection of >98% resulted in a significant survival advantage compared with a less complete resection [1]. Similarly, a statistically significant survival advantage was found for complete tumor resections achieved with intraoperative fluorescence for guidance [4, 5]. These results suggest that maintaining accurate registration between the patient in the OR and the available image data throughout the course of surgery is crucial to achieving the best possible surgical outcomes.

Techniques for establishing an accurate patient registration at the start of surgery are well studied. Most methods utilize fiducial markers either implanted in skull or affixed to scalp that allow a homologous set of points to be identified in the OR and spatially matched with their counterparts in the preoperative images. Matching skull-implanted fiducials usually yields the highest registration accuracy (~ 1 mm [6]) and is considered to be the “gold standard”; however, the invasiveness of the approach is often not justified given that intraoperative brain deformation can significantly compromise registration accuracy even at the start of a case. Consequently, registrations based on skin-affixed fiducials are more commonly employed in practice because of their simplicity and noninvasiveness, despite the relatively inferior registration accuracy (typically 2–5 mm in terms of fiducial registration error, FRE [7]; e.g., [8, 9]).

Although accurate patient registration is relatively easy and reliable to obtain before surgery, *maintaining* sufficient registration accuracy once surgery begins is a challenge for current commercial image-guidance systems because rigid body techniques are used to establish the spatial transformation; yet, the brain deforms as soon as the skull/dura is opened (e.g. due to loss of cerebrospinal fluid or release

of intracranial pressure from a space-occupying mass). This type of intraoperative brain deformation is commonly referred to as “brain shift”, and is widely recognized as the single most important barrier to maintaining an accurate image-to-patient registration throughout surgery. The magnitude of brain shift can reach 20 mm or more at the cortical surface [10, 11] and often exceeds 3 mm at the tumor margin [12]. In general, brain shift is dynamic (deformation is more significant as surgery progresses [13]), complex (brain motion does not necessarily correlate with gravity and the magnitude of movement is more significant in the hemisphere ipsi-lateral to the craniotomy [14]), and seemingly unpredictable. Because brain shift invalidates the registration on which neuronavigation is traditionally based, methods to estimate and compensate for intraoperative brain deformation are under development in order to maintain the accuracy required for image-guidance.

2 Image-Based Brain Shift Compensation

Various intraoperative imaging techniques have been used to compensate for brain deformation during surgery. The most dominant schemes are intraoperative magnetic resonance (iMR; e.g., [15–18]) and ultrasound (iUS; e.g., [19–23]) because they provide full or partial volume sampling of structures of interest deep in the brain. Although iMR provides unparalleled delineation of parenchymal tissue (e.g., [6, 12, 13]), its substantial capital cost, intrusion to neurosurgical workflow in the OR, and relatively long image acquisition time are practical barriers to its gaining wide acceptance. By comparison, iUS offers real-time image acquisition, is easy to implement, and is low in cost, but suffers from lower soft-tissue contrast and much greater operator dependence. When two-dimensional iUS is utilized, structures of interest may only be partially sampled because of discontinuous or limited image acquisition. Although three-dimensional (3D) reconstruction of a series of tracked freehand 2D iUS images may allow volumetric sampling of the region, constraints imposed by the craniotomy as well as line-of-sight from the tracking system often limit the volume acquisition. Volumetric true 3D iUS with a dedicated 3D US transducer is now possible in image-guided neurosurgery, which provides complete sampling of the region of interest with a single image acquisition [22]. However, iUS image noise, artifacts, and limited feature localization often make delineation of anatomical structures more difficult, especially when used alone. In practice, iUS is often coregistered with pMR which substantially improves the interpretation and understanding of the intracranial features captured with the technique.

Intraoperative stereovision (iSV [24–27]) and laser range scanning (e.g., [28–30]) optically acquire views of the exposed parenchymal surface allowing reconstruction of a full 3D surface profile of the surgical field with texture information. Surface feature displacements are then obtained by registering the reconstructed cortical surface with pMR (e.g., [25, 31]), or by tracking and registering surface

images directly over the course of surgery [26, 29, 30]. While these optical techniques noninvasively capture exposed surface profiles at any given time during surgery, they do not sample internal anatomical structures. Therefore, iSV or laser range scanning techniques alone may not be sufficient to accurately compensate for whole-brain deformation, especially when large displacements occur deeper in the brain (e.g., at later stages of surgery).

Intraoperative fluorescence imaging (iFI) is gaining attention as an approach to directly visualize surgical margins during tumor resection [32–34]. This technique provides the surgeon with a surface biomarker of disease through which a resection decision can be made based on the intensity of the fluorescing signature. In principle, the method is not vulnerable to tissue motion and may eliminate the need for image guidance once tumor resection begins. However, it is presently unable to provide navigational assistance prior to exposure of the tumor, and it only presents the surgeon with a surface map to indicate the presence of disease, but does not show the relative location of other structures of interest beyond the tumor. Thus, iFI alone seems unlikely to obviate the need for traditional image-guided neuronavigation or the need to compensate for intraoperative brain deformation.

The characteristics of various intraoperative imaging techniques alone are either impractical for routine use (e.g., iMR) or insufficient to provide whole-brain image updates for neuronavigation (e.g., iUS, iSV, laser range scanning, and iFI). One approach is to assimilate feature displacements sampled intraoperatively into a biomechanical model in order to generate whole-brain deformation through which a model-updated MR (uMR) is produced for subsequent neuronavigation. This chapter summarized the important aspects of a model-based approach for estimation of intraoperative brain deformation. First, we provide an overview of model-based brain shift compensation (Sect. 3), which is followed by discussion of a data assimilation inversion scheme (Sect. 4) and incorporation of contact brain-skull boundary conditions (BCs; Sect. 5). Techniques for generating displacements using iUS and iSV are described in order to guide model computation (Sect. 6). We further illustrate the use of iFI for validating model estimation of intraoperative brain deformation in order to maximize surgical benefit (Sect. 7). Finally, the clinical feasibility of the model-based brain shift compensation strategy is discussed in Sect. 8.

3 Model-Based Brain Shift Compensation

Biomechanical models are becoming increasingly important in estimating intraoperative brain deformation for improved accuracy in neurosurgical image-guidance, especially at early stages of surgery (e.g., [24, 35–42]). These models are typically subject-specific (i.e., geometry is constructed directly from patient's own pMR images) and incorporate specific loading and boundary conditions in the OR. Because brain shift during surgery is seemingly unpredictable and usually

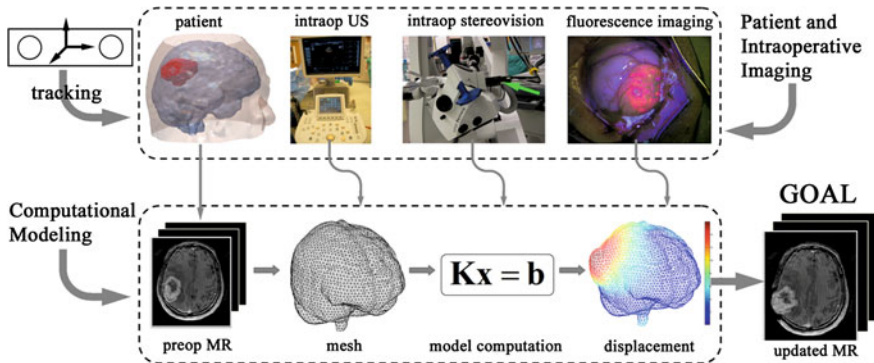


Fig. 1 Conceptual illustration of model-based brain shift compensation. The patient's head and intraoperative images (e.g., iUS, iSV, and iFI) are continuously monitored through a common tracking system. The resulting sparse displacement data are assimilated into a subject-specific biomechanical model to produce whole-brain deformation from which an updated MR volume is generated for subsequent neuronavigation

complex (e.g., [14]), computational models alone are not likely to be sufficiently accurate to predict intraoperative brain deformation without incorporating displacements measured intraoperatively.

Intraoperative parenchymal movement can be determined from anatomical structures deeper in the brain using iMR (e.g., [15, 35, 36, 43]) or iUS (e.g., [37, 44]) and/or from exposed cortical surface using stereovision [24, 45, 46] or laser range scanning [30, 40]. When displacement data are available both in the deeper brain and at the cortical surface, they can be combined to increase model solution accuracy (e.g., [47]). A typical schematic of model-based brain shift compensation is illustrated in Fig. 1, where the patient's head and intraoperative images (e.g., iUS, iSV, and iFI) are continuously registered by a common tracking system. The resulting displacement data are often sparse (i.e. information on parenchymal movement is captured only over part of the brain volume or the motion of discrete features is followed) and are assimilated into a subject-specific biomechanical model to estimate the whole-brain displacement field based on which an updated MR volume is generated for subsequent neuronavigation.

Intraoperative sparse displacements can be incorporated into the model either through a “forward” or an “inverse” scheme depending on how these data are utilized. In a forward scheme (also known as the “forced-displacement method”), the model is constrained to exactly match the measured information through boundary condition assignment [15, 24, 36, 43, 45]. The main advantage of this approach is its simplicity and computational efficiency. However, forcing the model to match exactly the measured displacement data may have some unintended consequences. For example, stress concentrations at otherwise stress-free locations (i.e., exposed parenchymal surface) can occur which may result in greater inaccuracies in regions away from the measurement data. In addition, the

technique introduces measurement noise directly into the brain deformation estimates that may be avoidable with other approaches [37, 48].

Inversion is another strategy that has been developed. Kobashi et al. [49] formulated the equations of mechanical motion in terms of known and unknown forcing conditions in which weighting factors are calculated in order to balance solution dependency on the forcing at observed and unobserved surfaces. Dumburi et al. [40] employed an atlas-based inversion method in which discrete values of variables that are important to brain shift (e.g., brain orientation, CSF drainage, drug administration, etc.) are combined to compute a set of model basis solutions prior to surgery. Intraoperatively, deformation of the brain is estimated through a least squares fitting to displacement observed during surgery to compute factors that combine the basis solutions in a weighted sum. They manually compared pre- and post-operative MR images to construct surface/subsurface displacement fields and used the surface results to drive the inverse model to validate its accuracy against subsurface displacement data in eight patient cases. Their results showed that 85% of the subsurface deformation was captured [40]. The approach is very attractive because the inversion is relatively simple to implement and fast to compute, although the amount of pre-operative computation grows exponentially when more variables and denser variations are considered. In addition, *extrapolation* (instead of interpolation) occurs if values of variables fall outside the range used pre-operatively, which increases model estimation uncertainty.

In parallel, our group has developed a data-guided compensation strategy in order to maintain image registration accuracy within the operative field. This inversion scheme iteratively estimates the right-hand-side forcing vector in order to minimize model-data misfit at intraoperatively determined measurement sites. Because model solution is guided by intraoperative motion measurements, the reliance on model prediction is significantly reduced. A summary of this data assimilation inversion scheme is presented in subsequent sections of the chapter.

4 Data Assimilation Through Inversion

We have used Biot's consolidation theory [50] to model the brain as a porous deformable medium in which pressure gradients from incompressible interstitial fluid flow act as a hydrodynamic driving force. While other important single and multi-phasic models (e.g. viscoelastic [51, 52], hyperelastic [53–55], etc.) have been developed for brain biomechanics, a detailed discussion of the relative merits of these formulations is beyond the scope of this chapter. Questions of linear versus non-linear constitutive laws are also of interest (and the motivated reader may refer to [36] for more discussion), but are likely to be of less importance here because a displacement-driven data assimilation approach is used. Instead, we focus on the estimation problem and, in principle, another material model or constitutive law could be substituted for the one we have used (although the

Table 1 Model parameters and their values

Parameter	Description	Value
G	Brain shear modulus	2100 Pa
N	Brain Poisson's ratio	0.46
ρ_t	Brain tissue density	1000 kg/m ³
$\rho_{f,s}^a$	Surrounding fluid density for saturated tissue	1000 kg/m ³
$\rho_{f,u}^a$	Surrounding fluid density for unsaturated tissue	1.0 kg/m ³
K	Hydraulic conductivity	1e ⁻⁷ m ³ s/kg
A	Ratio of fluid volume to change in solid volume	1
$1/S$	Fluid that can be forced into the tissue under constant volume	0
Ψ	Pressure source strength	0 Pa/s

^a ρ_f in Eq. 1 has either the value for $\rho_{f,s}$ or $\rho_{f,u}$ depending on whether the tissue is saturated or unsaturated with fluid

numerical characteristics of the estimation, for example its stability, would certainly change).

In our case, the governing equations of motion can be written as

$$\nabla \cdot G \nabla \mathbf{u} + \nabla \frac{G}{1 - 2\nu} (\nabla \cdot \mathbf{u}) - \alpha \nabla p = (\rho_t - \rho_f) \mathbf{g}, \quad (1)$$

$$\alpha \frac{\partial}{\partial t} (\nabla \cdot \mathbf{u}) + \frac{1}{S} \frac{\partial p}{\partial t} - \nabla \cdot k \nabla p = \Psi, \quad (2)$$

where \mathbf{u} and p represent the displacement and pore fluid pressure to be computed, respectively. Their numerical (finite element) solution is discussed in detail in [56]. Table 1 lists the corresponding material properties and typical values for brain obtained from the literature [57] that have been used successfully in any number of in vivo experiments (e.g. in a porcine brain retraction study described in [58]). Finite element discretization converts the two coupled equations into a linear algebraic system expressed in matrix form [56]:

$$\mathbf{Kx} = \mathbf{b}, \quad (3)$$

where \mathbf{K} is the stiffness matrix that encodes the discretized model equations, \mathbf{x} is the solution vector of displacement and pore fluid pressure (4 degrees-of-freedom, DOF, per node), and \mathbf{b} is the forcing vector that includes forces and boundary conditions associated with surgical intervention including interior forces such as those resulting from gravitational effects due to loss of tissue buoyancy during surgery. In addition, when brain-skull contact boundary conditions are used to capture interactions of the parenchymal surface with the skull, contact forces are also included (see Sect. 5 for more details [47]). For examples presented in the following sections, the brain was meshed into linear tetrahedral elements using methods in [59]. Other types of brain meshes (e.g., with hexahedral, see [60], or higher order elements) can also be used. These meshing and their associated algorithmic details fall outside the scope of this chapter.

4.1 The Adjoint Equations

When incomplete displacement measurements are available, a generalized inversion is suitable for minimizing the difference (ϵ) between the model estimate (\mathbf{x}) and measured data (\mathbf{d}) through a least-squares optimization constrained by the model equations (Eq. 3 [61]). The process is achieved by employing Lagrange multipliers that embed the model equations as constraints within the objective function. Specifically, data error and forcing condition covariance models and a set of Lagrange multipliers (λ) are introduced to form an augmented quadratic objective function, Ω [61],

$$\Omega = (\mathbf{d} - \mathbf{Ax})^T \mathbf{W}_\epsilon (\mathbf{d} - \mathbf{Ax}) + \mathbf{b}^T \mathbf{W}_b \mathbf{b} + \lambda^T (\mathbf{Kx} - \mathbf{b}), \quad (4)$$

where \mathbf{A} is a sampling matrix producing values of the computed solution at locations given by the measurement data. The matrices \mathbf{W}_b and \mathbf{W}_ϵ (inverses of the covariances of \mathbf{b} and ϵ , respectively) describe the covariances of the forcing conditions between any two locations and the data error between any two measurement points, and are controlled by the standard deviation in the correlation length (L) and the measurement error (σ_ϵ), respectively [37, 61]. The true covariance structures may not be known, but can be reasonably approximated. For \mathbf{W}_b , a distance-based model was employed [61] where an exponential decay based on the distance (r) between two points within an expected length (L) over which forcing conditions are correlated and the standard deviation (σ) in the expected size of the forcing condition are combined as

$$\text{cov}(b_i, b_j) = \sigma_i \sigma_j \left(1 + \frac{r}{L}\right) e^{-\frac{r}{L}}, \quad (5)$$

where (i, j) denotes the two locations. This model ensures that adjacent nodes will have similar values of \mathbf{b} , and the range over which they are similar is controlled by the correlation length, L . For \mathbf{W}_ϵ , the error in the data is assumed to be uncorrelated with uniform variance in the u_x , u_y , and u_z measurements, which leads to a diagonal matrix with elements being the reciprocals of the variances

$$\text{cov}(\epsilon_i, \epsilon_j) = \delta_{ij} \sigma_{\epsilon,i} \sigma_{\epsilon,j}, \quad (6)$$

where δ_{ij} is the Kronecker delta function and $\sigma_{\epsilon,i}$ is the standard deviation in the displacement measurement at location i .

By embedding the governing equations (i.e., Eq. 3) and covariance models into the objective function (Eq. 4), the constrained optimization is converted into an unconstrained problem. The objective function includes the unknown control variables \mathbf{b} and \mathbf{u} that must obey the biomechanical equations. The Lagrange multipliers, λ , are additional scalar variables that serve as the constraint weighting factors, adding to the list of unknowns. The value of each Lagrange multiplier denotes the resistance of the objective function minimum to violation of the constraint represented by the corresponding (discretized) equation of motion.

Using stationarity of the first-order conditions to determine the minimum of the objective function, the derivatives of Ω with respect to \mathbf{x} , \mathbf{b} and λ are set to zero, resulting in the following set of “adjoint equations” after some simplification (Eq. 10 rewrites the definition of the model-data misfit [37, 44, 61]):

$$\frac{\partial \Omega}{\partial \mathbf{x}} = \mathbf{K}^T \lambda - 2\mathbf{A}^T \mathbf{W}_\varepsilon \varepsilon = 0, \quad (7)$$

$$\frac{\partial \Omega}{\partial \mathbf{b}} = 2\mathbf{W}_b \mathbf{b} - \lambda = 0, \quad (8)$$

$$\frac{\partial \Omega}{\partial \lambda} = \mathbf{K}\mathbf{x} - \mathbf{b} = 0, \quad (9)$$

$$\varepsilon - (\mathbf{d} - \mathbf{A}\mathbf{x}) = 0. \quad (10)$$

These adjoint equations can be solved directly using the Representer algorithm (REP) [37], which essentially tests the response of the model to a unit misfit at each data point and generates a weighted sum of these solutions to minimize the objective function (Eq. 4). The algorithm produces a direct solution (i.e. no iteration) and is relatively simple to implement. However, its computational complexity grows linearly with the number of sparse data points, N_{sps} , and the computational costs can become impractical (in the OR) when N_{sps} is large (e.g., when sparse displacement data are generated from true 3D iUS).

4.2 Steepest Gradient Descent

In order to assimilate large amounts of sparse data points, we developed an iterative solution to Eqs. 7–10 based on steepest gradient descent (SGD). This algorithm adjusts the forcing vector to search for the minimum of the scalar function (Ω) within the multidimensional space, \mathbf{b} . If the forcing vector at the k th iteration is \mathbf{b}_k , it is updated at the next iteration as

$$\mathbf{b}_{k+1} = \mathbf{b}_k + \Delta \mathbf{b}, \quad (11)$$

where the change in the forcing conditions, $\Delta \mathbf{b}$, is separated into its directional ($\hat{\partial} \mathbf{b}$) and magnitude (α) components. Using the steepest gradient, the directional component is determined through

$$\hat{\partial} \mathbf{b} = -\hat{\partial} \Omega / \hat{\partial} \mathbf{b}, \quad (12)$$

which specifies a line in the n -dimensional space (n is the total number of motion constraint equations in Eq. 3) along which the minimum of the scalar function, Ω , is sought. The magnitude of the forcing vector adjustment, α , selects the distance along this direction that the update is projected in the next iteration. First, the effect of an incremental change in the forcing vector, \mathbf{b} , is defined as

$$\partial \mathbf{x} = [\mathbf{K}^{-1}] \partial \mathbf{b} \text{ and } \partial \varepsilon = -[\mathbf{A}] \partial \mathbf{x}, \quad (13)$$

which are linearly related to the magnitude, β , through

$$\Delta \mathbf{b} = \beta \times \partial \mathbf{b}, \quad (14)$$

$$\Delta \mathbf{x} = [\mathbf{K}^{-1}] \Delta \mathbf{b} = [\mathbf{K}^{-1}] \beta \times \partial \mathbf{b}, \text{ and} \quad (15)$$

$$\Delta \varepsilon = \beta \times \partial \varepsilon. \quad (16)$$

Consequently, the value of the objective function, Ω , at the $(k + 1)$ st iteration is given by

$$\begin{aligned} \Omega_{k+1} &= (\varepsilon_k + \Delta \varepsilon)^T \mathbf{W}_\varepsilon (\varepsilon_k + \Delta \varepsilon) + (\mathbf{b}_k + \Delta \mathbf{b}) \mathbf{W}_b (\mathbf{b}_k + \Delta \mathbf{b}) \\ &= \Omega_k + \Delta \varepsilon^T \mathbf{W}_\varepsilon \varepsilon_k + \varepsilon_k^T \mathbf{W}_\varepsilon \Delta \varepsilon + \Delta \varepsilon^T \mathbf{W}_\varepsilon \Delta \varepsilon \\ &\quad + \Delta \mathbf{b}^T \mathbf{W}_b \mathbf{b}_k + \mathbf{b}_k^T \mathbf{W}_b \Delta \mathbf{b} + \Delta \mathbf{b}^T \mathbf{W}_b \Delta \mathbf{b}. \end{aligned} \quad (17)$$

Assuming $[\mathbf{W}_b]$ and $[\mathbf{W}_\varepsilon]$ are symmetric, Eq. 17 is further simplified to

$$\begin{aligned} \Delta \Omega &= 2\beta \cdot (\partial \varepsilon^T \mathbf{W}_\varepsilon \varepsilon_k) + \beta^2 \cdot (\partial \varepsilon^T \mathbf{W}_\varepsilon \partial \varepsilon) \\ &\quad + 2\beta \cdot (\partial \mathbf{b}^T \mathbf{W}_b \mathbf{b}_k) + \beta^2 \cdot (\partial \mathbf{b}^T \mathbf{W}_b \partial \mathbf{b}). \end{aligned} \quad (18)$$

The optimal scalar magnitude is then determined by setting $\partial \{\Delta \Omega\} / \partial \beta = 0$, leading to

$$\beta = - \frac{\{\partial \mathbf{b}\}^T [\mathbf{W}_b] \{\mathbf{b}\} + \{\partial \varepsilon\}^T [\mathbf{W}_\varepsilon] \{\varepsilon\}}{\{\partial \mathbf{b}\}^T [\mathbf{W}_b] \{\partial \mathbf{b}\} + \{\partial \varepsilon\}^T [\mathbf{W}_\varepsilon] \{\partial \varepsilon\}}, \quad (19)$$

which dictates the amount of forcing vector advancement along the line parallel to $\partial \mathbf{b}$. The overall solution process is represented by the following pseudo algorithm:

1. Initialize stiffness, covariance and sampling matrices $([\mathbf{K}], [\mathbf{W}_\varepsilon]^{-1}, [\mathbf{W}_b]^{-1}, [\mathbf{A}])$.
2. Compute the best prior estimate of \mathbf{b} ; set to $\mathbf{0}$ if unavailable.
3. Solve the forward model for \mathbf{x} : $\mathbf{Kx} = \mathbf{b}$.
4. Sample the model-data misfit: $\varepsilon = \mathbf{d} - \mathbf{Ax}$.
5. Solve the adjoint model for λ : $[\mathbf{K}]^T \lambda = 2[\mathbf{S}^T \mathbf{W}_\varepsilon] \varepsilon$.
6. Evaluate $\nabla \Omega$ with respect to \mathbf{b} ; $\mathbf{g} = 2[\mathbf{W}_b] \mathbf{b} - \lambda$; STOP if $\|\mathbf{g}\| \approx 0$.
7. Set the direction of descent (steepest gradient descent): $\partial \mathbf{b} = -\mathbf{g}$.
8. Project in the resulting direction: (a) $\partial \mathbf{x} = [\mathbf{K}]^{-1} \partial \mathbf{b}$; (b) $\partial \varepsilon = -[\mathbf{A}] \partial \mathbf{x}$.
9. Set the step size: $\beta = - \frac{\{\partial \mathbf{b}\}^T [\mathbf{W}_b] \{\mathbf{b}\} + \{\partial \varepsilon\}^T [\mathbf{W}_\varepsilon] \{\varepsilon\}}{\{\partial \mathbf{b}\}^T [\mathbf{W}_b] \{\partial \mathbf{b}\} + \{\partial \varepsilon\}^T [\mathbf{W}_\varepsilon] \{\partial \varepsilon\}}$.
10. Assemble increments: $\mathbf{b} = \mathbf{b} + \beta \times \partial \mathbf{b}$.

The most computationally intensive steps (3, 5 and 8a) involve the solution of full linear systems of equations ($3 \times Iter$ equations in total for $Iter$ iterations). The number of sparse data points used to construct the estimate of \mathbf{b} only affects the computation of the model-data misfit (step 4) and the calculation of the effect of $\delta\mathbf{x}$ on the misfit (step 8b). Thus, the computational costs increase marginally with the increase in N_{sprs} because no change in the rank of the full linear systems of equations is involved. Therefore, the overall solution computation with SGD does not scale directly with N_{sprs} . Since the linear least squares formulation has a single minimum, SGD will converge to the correct minimum, although the convergence rate may be slow which necessitates the use of a practical stopping criterion to terminate the iteration in order to achieve sufficient accuracy in the model estimate with minimum computational costs [61]. The minimum number of iterations ($Iter_{min}$) needed to reach an approximate convergence of SGD can be empirically defined to occur when the change in the model-data misfit relative to the previous iteration is less than 0.1% of the initial model-data misfit (ε_{init}), or formally

$$Iter_{min} = \min(k) \text{ such that } \|(\varepsilon_{sprs}^k - \varepsilon_{sprs}^{k-1})\| < 0.001 \times \varepsilon_{init}, \quad (20)$$

where ε_{sprs}^k refers to ε_{sprs} achieved at the k th iteration ($k > 1$), and ε_{init} is the initial model-data misfit [47].

In order to evaluate the performance of the SGD algorithm, we compared model-data misfit results with those obtained from the REP in five representative neurosurgical cases in which intraoperative tumor displacements measured after dural opening were assimilated. Sparse data points randomly selected from the measured tumor displacements ($N_{sprs} = 10, 100, \text{ and } 200$) were used for model guidance. Model-data misfit at sparse data locations (ε_{sprs}) and cross-validation positions (ε_{cross} ; defined as measurements not selected for model guidance) were quantitatively compared. The number of iterations for SGD was determined as the minimum iteration at which ε_{sprs} generated from SGD was statistically equal to or smaller than that generated from REP.

Figure 2a demonstrates that model solution accuracy improves with the increase in the number of data points used for model guidance for both SGD and REP algorithms. With sufficient sparse data, SGD is able to attain model estimates comparable to or better than those obtained with REP, capturing about 74 to 82% of tumor displacement (Fig. 2b). Although the run times of both SGD and REP increased with the increase in N_{sprs} , the normalized execution time of SGD relative to that of REP decreased significantly, resulting in a fourfold or more reduction relative to REP when N_{sprs} is large (Fig. 3).

In order to further reduce the computational costs of solutions of linear systems of equations that are the most computationally intensive in both SGD and REP algorithms, a multithreaded direct solver, PARDISO [62], was employed. This solver explicitly factorizes the system matrix and uses forward elimination and backward substitution to complete the solution process [63], thereby eliminating the need for any iterative solvers (e.g., SPLIB [64]). With the PARDISO direct

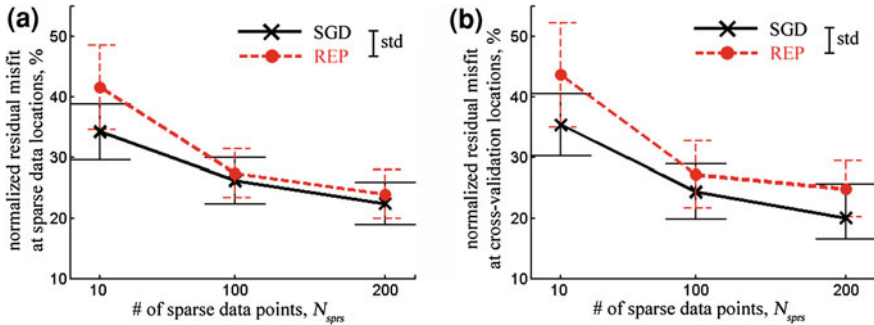


Fig. 2 Model-data misfit $\varepsilon_{\text{sprs}}$ **(a)** and $\varepsilon_{\text{cross}}$ **(b)** normalized with respect to the initial misfit, $\varepsilon_{\text{init}}$, as a function N_{sprs} for the pooled clinical datasets. For both SGD and REP, normalized $\varepsilon_{\text{sprs}}$ and $\varepsilon_{\text{cross}}$ decreased with the increase in N_{sprs}

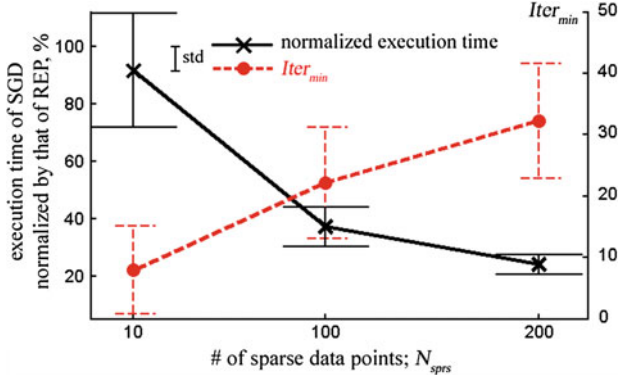


Fig. 3 Using the pooled datasets, the normalized run-time of SGD relative to REP decreased when N_{sprs} increased. Also shown are the minimum iterations required for SGD to reach an $\varepsilon_{\text{sprs}}$ statistically equal to or less than that produced by REP (dashed line) for each N_{sprs}

solver on a shared-memory eight-processor Linux cluster (8G RAM in total and 2.33 GHz for each processor) which is readily accessible to the OR, an average computational cost of ~ 2 min for estimating whole-brain deformation can be achieved with SGD using 100 sparse data points, demonstrating that this algorithm is sufficiently fast with adequate accuracy for routine clinical use [38].

Conjugate gradient descent (CGD) is also possible and can be used to solve the same set of adjoint equations, which is likely to improve the computational efficiency of the inversion scheme because solution of the forward model is not required during iteration [61]. However, solution of the forward problem during the iteration in SGD (i.e., step 3 in the algorithm) actively adjusts the right-hand side forcing conditions which effectively allows contact forces to be incorporated when brain node penetration occurs in the brain-skull contact BCs described in the

next section. When brain-skull contact BCs are not expected to significantly improve model solution accuracy (e.g., when the brain is fully distended towards the skull), CGD is recommended to gain the additional computational efficiency.

5 Brain-Skull Contact Boundary Conditions

Boundary conditions (BCs) are important inputs for accurate brain deformation estimation. One challenge is representing the brain-skull interactions because the parenchyma around the craniotomy may move towards or away from the rigid skull once the dura is opened. For example, portions of the cortical surface may initially distend and then relax and collapse over time. Therefore, assigning fixed brain-skull BCs (e.g., [37, 44, 45, 57, 58]) will not accommodate the dynamic nature of brain-skull interaction. One approach to solve this problem is to implement contact BCs [24] that allow nodes representing the parenchymal surface to move freely unless they are in contact with the skull.

5.1 Contact BC Formulation

We have incorporated brain-skull contact BCs through a penalty method applied to surface nodes initially assigned as potentially in contact (i.e., slave nodes; usually those in the neighborhood of the craniotomy site) with the inner-surface of the skull (i.e., master surface). The motion of these slave nodes is tracked during iterative model solution to maintain an impenetrability condition through a penalty method based on an efficient three-step contact search algorithm. With this approach, the contact problem becomes one of minimizing the initial total body potential energy subject to the penetration constraints. A penalty function is introduced when slave node penetration occurs which applies an opposing force proportional to the penetration distance to keep the node from crossing the skull boundary.

Schematically, the closest point projection or the contact point with the master surface, Γ_m , is obtained for any slave node, s , through a three-step contact search algorithm (Fig. 4) [65]. First, the slave node's closest master node (m) and the neighboring master elements are identified. Then, the slave node's projection points on the resulting elements are computed and the one closest to s and within the elemental border is denoted as the closest point projection. When no valid projection is returned (e.g., due to nonconvexity), the closest element edge is considered. If no projection point is within the corresponding end points, the closest master node, itself, is used as the contact point. To alleviate the difficulty when searching for a contact point in nonconvex regions such as the basal region of the skull, the range of the neighboring master elements is recursively expanded.

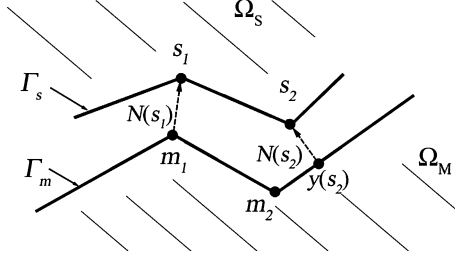


Fig. 4 Illustration of a one-body frictionless contact against a fixed rigid body. The contact boundaries of the deformable (Ω_s) and rigid body (Ω_m) domains are defined as the slave (Γ_s) and master (Γ_m) surfaces, respectively. For a given slave node (s), its contact point on the master surface ($y(s)$) is determined through a three-step contact search algorithm [65], and the local master surface normal at the contact point ($N(s)$) is subsequently calculated

The resulting contact point, $y(^0s)$, serves as the reference for determining slave node penetration, which, at time zero before deformation, is given by

$${}^0p = (y(^0s) - {}^0s) \cdot N(^0s), \quad (21)$$

where $N(^0s)$ is the initial local master surface normal at the contact point prior to deformation. At time t after deformation, the penetration is updated to account for displacement of a slave node

$${}^t p = ({}^t x - {}^s x) \cdot N(^t s) + (y(^0s) - {}^0s) \cdot N(^0s) = -{}^s x \cdot N(^t s) + {}^0p, \quad (22)$$

where ${}^s x$ and ${}^t x$ are displacements of the slave node and its corresponding contact point (${}^t x = 0$ when the master surface is fixed), respectively, and $N(^t s)$ is approximated by $N(^0s)$ assuming small changes occur in the master surface normal ($N(^t s) = N(^0s)$, when the master surface is fixed). The kinematical impenetrability condition for slave node, s (i.e., so s does not penetrate through the master surface), is given by [66, 67]

$${}^t p = -{}^s x \cdot N(^0s) + {}^0p \leq 0, \quad (23)$$

leading to the matrix form for assembling L ($L \geq 1$) slave nodes

$$\mathbf{P} = \mathbf{Qx} + {}^0\mathbf{P} \leq 0, \quad (24)$$

where \mathbf{Q} is a $dim \times L$ (dim equals 2 or 3 for a two- or three-dimensional problem, respectively) matrix of L diagonal submatrices with diagonal elements, q_{ij} , in each submatrix given as

$$q_{ij} = -N_j(s_i). \quad (25)$$

The subscripts in Eq. 25 denote the j th local master surface normal component ($j = 1, dim$) for the i th slave node ($i = 1, L$).

When a slave node penetrates through the master surface, a force normal to the master surface is generated with a magnitude proportional to the penetration depth, which satisfies the kinematical impenetrability condition (Eq. 24), and is applied at the contact point using a penalty method. Effectively, the total body potential energy of the system is rewritten to account for these contact forces

$$\Pi_p(\mathbf{x}) = \Pi + \pi_p = \frac{1}{2}\mathbf{x}^T \mathbf{K} \mathbf{x} - \mathbf{x}^T \mathbf{b} + \frac{1}{2}\mathbf{P}^T \beta \mathbf{P}, \quad (26)$$

where each term represents the component of total body potential energy due to internal, external and contact forces, respectively. The penalty coefficient, β , is a diagonal matrix ($\beta_{ii} > 0$; $i = 1, \dots, \dim \times L$) that controls the magnitude of the contact forces. The exact impenetrability condition is only achieved when $\beta \rightarrow \infty$, which is not possible in practice because of matrix ill-conditioning [66]. If β is too large, the matrix solution becomes unstable, whereas if β is too small, slave nodes penetrate the master surface too far, which is also undesirable. An empirical value of 5 (i.e., $\beta_{ii} = 5$, for $i = 1, \dots, \dim \times L$) has been suggested from previous investigations that led to reasonable performance [65]. To solve the system of equations, the total body potential energy is minimized which leads to

$$\frac{\partial \Pi}{\partial \mathbf{x}} = 0. \quad (27)$$

Combining Eqs. (24), (26) and (27) produces the modified system of equations (setting the penetration, \mathbf{P} , to zero in Eq. 24 [67]):

$$\mathbf{K}_p \mathbf{x} = \mathbf{b}_p, \quad (28)$$

where $\mathbf{K}_p = \mathbf{K} + \mathbf{Q}^T \beta \mathbf{Q}$ and $\mathbf{b}_p = \mathbf{b} - \mathbf{Q}^T \beta^0 \mathbf{P}$. Essentially, both sides of the model equation (i.e., Eq. 3) are reformulated to include the penalty terms due to slave node penetration.

5.2 Incorporating Contact BCs with SGD Inversion

The difficulty in resolving the contact constraints (Eq. 24) stems from the fact that the contact nodes, and hence, contact forces, are not generally known a priori. Therefore, a fully implicit trial-and-error approach was employed that iteratively solves the system of equations (Eq. 28) until the set of contact nodes is stable [68]. In a forward solution, steady state in the contact system is typically achieved in less than ten iterations when an empty initial set of contact nodes is used [65]. A similar iterative process occurs during SGD for minimizing the model-data misfit (see Sect. 4.1 for details [38, 61]). At the onset of each iteration, a forward model solution is computed to adjust the displacement estimate subject to the updated forcing conditions. With contact BCs, forces normal to the skull are generated when slave node penetration occurs. Essentially, these contact forces act as additional perturbations to the system forcing conditions obtained from SGD.

Thus, a second forward model is computed with the reformulated system of equations (Eq. 28). However, instead of using multiple forward solution iterations to stabilize the set of contact nodes within each SGD update, which would increase computation time significantly and limit practical application in the OR, only one contact iteration is performed within each SGD advance, and the slave node penetrations are resolved over the course of multiple SGD iterations. Consequently, the number of system solutions required to solve the model estimation problem with contact constraints is increased by one per SGD iteration, if contact nodes are detected.

These considerations lead to the identical algorithmic flow as the SGD framework, except that after step (3), the contact impenetrability condition, Eq. 28, is enforced by adjusting the solution vector, \mathbf{u} (only model displacement estimation is considered), and the right-hand side forcing vector, \mathbf{b} .

Implementation of the brain-skull contact BCs within the SGD inversion was verified by modeling brain sagging due to gravitation. A ground-truth displacement field was first generated using a forward model by assigning brain surface nodes around the craniotomy as in contact with the skull. Sparse displacements were then sampled on the tumor boundary near the craniotomy and used in the inverse model with the same brain-skull contact BCs. The SGD inversion algorithm successfully recovered whole-brain deformation after 14 iterations. As expected, model-data misfit was the smallest around the tumor boundary where sparse data were generated for model guidance [47].

Clinical application of brain-skull contact BCs was demonstrated in patient cases where model solutions generated from both contact and fixed BCs were compared. The same set of sparse displacement data sampled around the cyst boundary from coregistered intraoperative ultrasound images were used for model guidance, whereas the cortical surface profile independently determined from coregistered intraoperative stereovision was employed for cross-validation of the accuracy in model estimation of brain deformation (see Sect. 6 for details on generating sparse displacement data from intraoperative images). Figure 5 illustrates model-estimated displacements for one patient using the two types of brain-skull BCs. Clearly, model solution accuracy with the contact BCs far exceeds that with the fixed BCs for this patient case as indicated by the agreement between the model-estimated cortical surface profile and the one independently measured from iSV. In addition, a sagging response generated by the contact BCs (thick arrow in Fig. 6a) was lacking with the fixed BCs, as expected. These results demonstrate that the contact BCs significantly improve model estimation accuracy at the craniotomy (1.6 mm on average), especially when the parenchymal motion normal to the skull is large. They also suggest that the contact BCs allow more flexible representation of the brain-skull interface and that model performance significantly improves when brain-skull contact influences the deformation field but does not degrade when the contact is otherwise less critical and simpler BCs would suffice [47]. This algorithmic behavior is essential to robust operation in the OR.

A representative curve of cross validation errors ($\varepsilon_{\text{cross}}$) generated from the contact and fixed BCs in relation to inverse iteration count is illustrated in Fig. 6

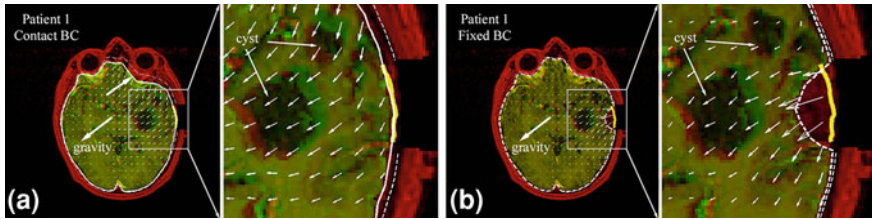


Fig. 5 Comparison of model-generated whole-brain deformation (green) using contact (a) and fixed (b) BCs for a patient whose parenchyma completely sagged at the craniotomy. Sparse data around the cyst were assimilated to guide the model. Thick yellow lines: cross-section of cortical surface acquired from coregistered iSV; Solid/dashed white lines: cross-sections of model-updated brain surface generated by the contact/fixed BCs; Thin dashed white lines: skull inner-surface

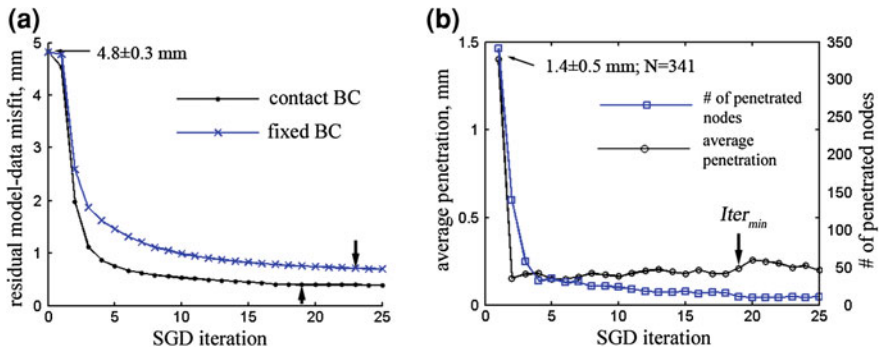


Fig. 6 Cross validation errors, $\varepsilon_{\text{cross}}$, for contact and fixed BCs (a) and number and average penetration distance (b) of contact nodes versus iteration count in a patient case where the parenchyma fully contracted at the craniotomy. The number of penetration nodes drops essentially to zero and $\varepsilon_{\text{cross}}$ improves with the contact BCs

for a patient whose parenchymal surface at the craniotomy fully contracted. The number of penetrating nodes virtually diminishes to zero using the contact BCs, suggesting fulfillment of the contact impenetrability condition. The average computational cost to reach convergence using the contact BCs is currently 3.9 min.

6 Intraoperative Sparse Displacement Data

Because of data assimilation, intraoperative sampling of parenchymal displacements is important to the overall clinical feasibility of the model-based brain shift compensation scheme. Displacements from either internal anatomical structures or exposed cortical surface can be utilized for model guidance, and the two sources of

intraoperative data are complementary as they often sample the parenchyma at spatially different locations during the same surgical stage. In practice, both sources of intraoperative displacements (when available) can be utilized, which is expected to improve model estimation accuracy because of the often rather complex and unpredictable nature of intraoperative brain deformation [14]. Typically, movement of internal features is derived from iUS whereas motion of the exposed cortical surface is obtained from iSV (or laser range scanning). In the following sections, we illustrate the techniques we have developed to derive feature displacements from iUS and iSV for the purpose of data assimilation.

6.1 Sparse Data from 2D iUS

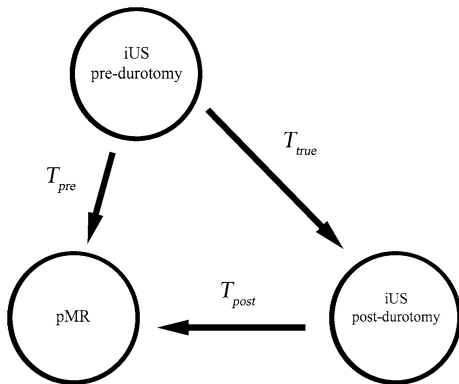
Measuring parenchymal displacements with iUS is conceptually straightforward because features of interest are captured with a single imaging modality and displacement mapping is essentially a registration to match features (e.g., tumor) at different points in time. With 2D iUS, however, a direct intramodality registration is not always possible between two arbitrary acquisitions because of limited sampling and gaps between image planes. Alternatively, an *indirect* approach that registers iUS with pMR sequentially can be used to match features in 2D iUS acquired at two surgical stages (e.g., before and after dural opening).

Using fiducial-based patient registration as the initial starting point, iUS images before dural opening are first re-registered with pMR (e.g., based on a technique we developed previously that employs normalized mutual-information as its image similarity measure [69]) in order to minimize tumor boundary misalignment between the two image modalities (T_{pre} in Fig. 7). Effectively, the image re-registration before dural opening collectively corrects transformation errors due to, for example, patient registration and US transducer calibration (assuming negligible tumor movement before dural opening). With the corrected inter-image registration, iUS after dural opening is again re-registered with pMR, and the resulting transformation characterizes tumor displacement due to dural opening. A displacement map is then obtained by applying the inverse of the resulting transformation (i.e., T_{post}^{-1} in Fig. 7) to the segmented pMR tumor boundary points. Effectively, the “true” transformation between iUS images before and after dural opening is determined from two successive registrations between iUS and pMR (the latter of which serves as a reference template) using

$$T_{\text{true}} = T_{\text{post}}^{-1} \times T_{\text{pre}}. \quad (29)$$

The combined computational cost of automatic image pre-processing and the two iUS-pMR registrations was typically around 3 min, suggesting that the technique is feasible for clinical applications in the OR. A potential challenge with this approach, however, lies in the robustness of registration between 2D iUS and pMR because of their underlying differences in imaging mechanisms that often

Fig. 7 Schematic of sequential registrations between iUS and pMR. Registration between iUS pre- and post-durotomy is determined sequentially registering with the reference template, pMR



lead to relatively small translational and rotational capture ranges (e.g., 5.9 mm and 5.2°, respectively [69]). Additionally, nonrigid registration between 2D iUS and pMR becomes more challenging because of the significant increase in the degrees-of-freedom. Therefore, using pMR as a reference template for successive rigid registration with iUS is likely to be limited to the early stages of surgery (e.g., after dural opening) when a rigid displacement map is sufficient for data assimilation. In the next section, we show that this limitation can be overcome by sampling the region of interest with true 3D iUS images that allow direct registration between US image volumes acquired at different surgical stages. Because a pMR reference volume is no longer needed, nonrigid registration is also possible between two 3D iUS image volumes, making this imaging modality ideal for generating intraoperative sparse displacement maps in the deeper brain.

6.2 Sparse Data from Volumetric True 3D iUS

6.2.1 Image Rasterization

Three-dimensional US provides full-volume sampling of the region of interest, which makes it possible to register acquisitions obtained at different points in time directly without the aid of pMR as a reference template. Reconstructed 3D iUS typically requires a series of tracked freehand 2D iUS images to be acquired with sufficient sampling of the region of interest [70, 71] to which algorithms using voxel-, pixel-, and function-based methods [72, 73] are often applied to interpolate image intensities at a set of regularly spaced rectilinear grid points.

Alternatively, volumetric true 3D iUS images recorded with a dedicated 3D transducer (e.g., X3-1 broad-band matrix array) are attractive for compensating for brain shift because a single volumetric acquisition fully samples the parenchymal region under the craniotomy [22, 74]. Because voxels in 3D iUS image volumes are arranged in a pyramid-shaped coordinate system (rather than a rectilinear

Cartesian grid), existing software packages are not directly applicable for image processing. Instead, rasterization is necessary which essentially interpolates image intensities at a set of rectilinear grid points. To maximize interpolation accuracy and computational efficiency, a trilinear interpolation scheme was developed that performs interpolation in a rectilinear parametric space rather than in the physical space of the native image volume [75]. With simulated, phantom and clinical image volumes, we have shown that this technique out performs both voxel nearest-neighbor and distance-weighted algorithms in terms of accuracy with a computational efficiency comparable to the fastest nearest-neighbor interpolation for processing tracked 2D ultrasound images (0.035 s per 2D cross-sectional image with 0.46 ms/1000 pixels and 1.05 s per full volume with a 1-mm³ voxel size with 0.23 ms/1000 voxels).

Additionally, multiple tracked volumetric 3D iUS images acquired at the same surgical stage can be merged into a single volume to offer expanded (and uniform) sampling through registration and interpolation. Because of errors due to tracking and/or US transducer probe calibration, misalignment can occur between homologous parenchymal features when two 3D iUS image volumes are spatially merged. To ensure the consistency of the merged image content in overlapping regions, these 3D iUS image volumes were rigidly re-registered via maximization of MI using an arbitrary image (e.g., the first image acquired) as the stationary template. Interpolation was found to be approximately 20% more accurate in overlapping regions when re-registration was performed and minimized feature loss and/or blurring that was evident without re-registration [76]. Apparently, the total computational cost increases linearly with the number of 3D iUS acquisitions involved (average time to combine and rasterize one pair of 3D iUS images was 1.5 s) if performed sequentially. With parallelization, however, the total computation time may not significantly increase because the registrations are independent of each other.

6.2.2 Generation of Sparse Displacement

With true 3D iUS image volumes, direct intramodality registrations extract feature displacement maps with average translational and rotational capture ranges (35.2 mm and 38.5°, respectively [76]) that are much larger than those when registering US and pMR (5.9 mm and 5.2°, respectively [69]). Similarly with 2D iUS, a “last-known” correct registration is first established between 3DUS and pMR before dural opening in order to collectively correct any misalignment between tumor (and/or feature) boundaries due to errors in patient registration and US transducer calibration. This registration is important because it defines the spatial transformation required to transform sparse displacement data from the 3D iUS image space into the pMR image space.

In order to compute feature displacements, a typical 3D iUS image volume acquired at a later surgical stage is spatially transformed into the image space of the 3D iUS image volume obtained before dural opening (i.e., chosen as the fixed

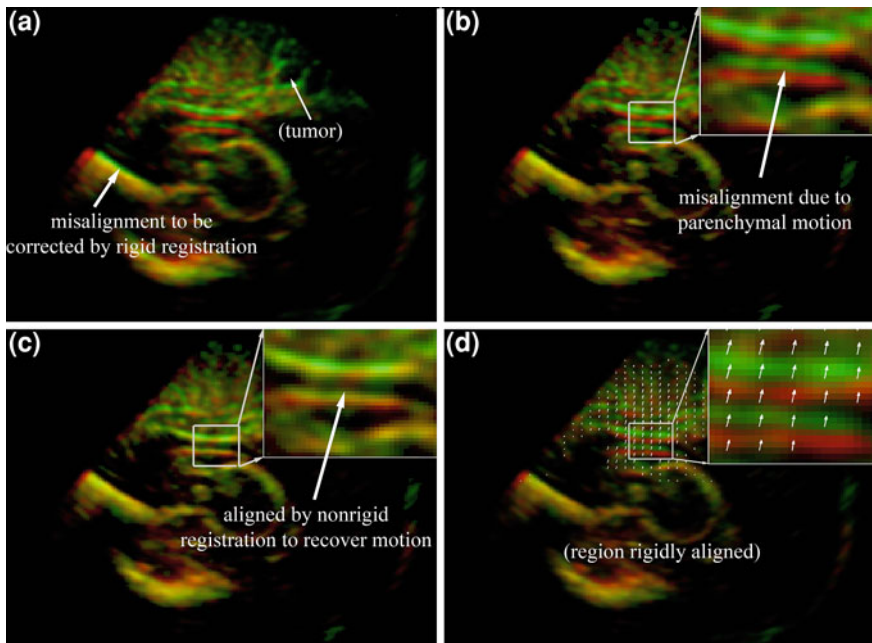


Fig. 8 Overlays of 3D iUS before (red) and after (green) dural opening using transforms obtained from the optical tracking (a) or rigid body re-registration (b). Feature alignment was significantly improved after B-Spline nonrigid registration (c), suggesting the effectiveness of the registration technique in capturing feature displacement. The resulting parenchymal feature displacement vectors are shown in d

image volume in registration) using the transformation provided by the tracking system. Because of errors in 3D iUS image acquisition and tracking, stationary or immobile features may be misaligned, which potentially degrade accuracy in the feature displacement measurements (e.g., parenchymal boundaries contralateral to the craniotomy/US transducer; see Fig. 8a). To compensate for this misalignment, a simple rigid body registration can be performed between the two image volumes by limiting the region of interest to the stationary features. In practice, portions of the image volume contralateral to the US transducer (i.e., corresponding to stationary features) are employed for image re-registration purposes. The two 3D iUS image volumes are then re-aligned, and any residual feature misalignment directly indicates tissue deformation (see Fig. 8b). Depending on the severity of nonrigid deformation, either a rigid (e.g., after dural opening; fast and robust but less accurate) or a nonrigid (e.g., after partial or complete tumor resection; slow but likely more accurate) registration can be performed between the two 3D iUS image volumes after rigid re-registration (based on the stationary features). A B-spline nonrigid registration may be preferred because it provides a smooth deformation field that is desirable when assimilating the displacement data to estimate whole-brain deformation. Figure 8c illustrates feature alignment after

nonrigidly registering two 3D iUS image volumes, and Fig. 8d shows the resulting displacement vectors in areas under the craniotomy where parenchymal distension was evident.

Because of the higher cost of computations with nonrigid registration, only the region of interest (e.g., around tumor or ventricles) is used for registration (where automatic and efficient segmentation of iUS is achievable), or a partial region under the craniotomy (e.g., scan depth between 1 and 6 cm instead of the full volume). Based on the displacement mapping, a randomly generated subset of voxels (e.g., $N = 200$) that are representative of the regional deformation can then be produced for data assimilation to further reduce the computational overhead.

6.3 Intraoperative Stereovision

6.3.1 Cortical Surface Reconstruction from iSV

Stereovision is another important intraoperative imaging technique that captures a texture intensity-encoded profile of the exposed cortical surface during surgery. Techniques for stereo image calibration and reconstruction based on a pinhole camera model and radial lens distortion correction can be found, e.g., in [25], and are briefly outlined here. A 3D point in world space (X, Y, Z) is transformed into the camera image coordinates (x, y) using a perspective projection matrix

$$\begin{pmatrix} x \\ y \\ 1 \end{pmatrix} = \begin{pmatrix} \alpha_x & 0 & C_x & 0 \\ 0 & \alpha_y & C_y & 0 \\ 0 & 0 & 1 & 0 \end{pmatrix} \times \mathbf{T} \times \begin{pmatrix} X \\ Y \\ Z \\ 1 \end{pmatrix}, \quad (30)$$

where α_x and α_y incorporate the perspective projection from camera-to-sensor coordinates and the transformation from sensor-to-image coordinates, (C_x, C_y) is the image center, while \mathbf{T} is a rigid body transformation describing the geometrical relationship between the two cameras. A total of 11 camera parameters (6 extrinsic: 3 rotation and 3 translation; and 5 intrinsic: focal length, f , lens distortion parameter, k_1 , scale factor, S_x , and image center, (C_x, C_y)) are determined through calibration using a least squares approach.

Stereo image rectification was employed to establish epipolar constraints that limit the search for correspondence points along “epipolar lines” (defined as the projection of the optical ray of one camera via the center of the other camera following a pinhole model). In addition, images are rotated so that pairs of epipolar lines are co-linear and parallel to image raster lines in order to facilitate stereo matching (see Fig. 9a, b for the two rectified images). An intensity-based correlation metric and a smoothness constraint were used to find the correspondence points. Each pair of correspondence points was then transformed into its respective 3D camera space using the intrinsic parameters, and transformed into a common

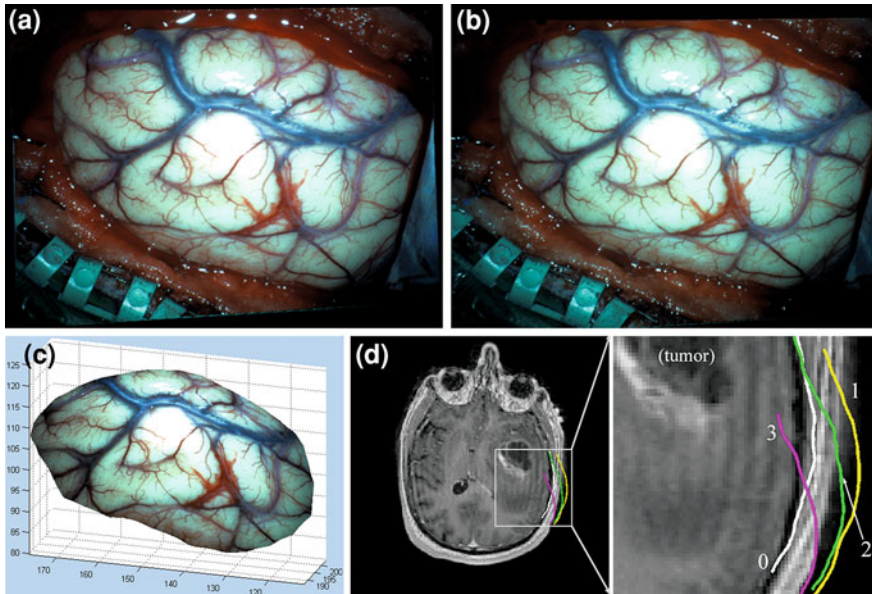


Fig. 9 Illustration of stereovision surface reconstruction: rectified left (a) and right (b) camera images after dural opening, which limit the search for correspondence points along a horizontal line. The reconstructed 3D cortical surface is shown in pMR image space (c). Cross-sections of a representative pMR axial image with respect to the reconstructed cortical surfaces (tumor cavity wall not included) are shown for four distinct surgical stages: (0) before dural opening; (1) after dural opening; (2) right before the start of tumor resection; and (3) after tumor resection in **d**

3D space using the extrinsic parameters. Together with their respective camera centers in the common space, two optical rays were constructed with their intersection defining the 3D location of the correspondence point pair (Fig. 9c). Figure 9d shows the cross-sections of a representative pMR axial image with respect to the reconstructed cortical surfaces at four distinct stages of surgery, which clearly demonstrate dynamic evolution of the cortical surface profile relative to pMR during the course of surgery.

6.3.2 Deriving Sparse Data from iSV

Similarly to iUS, generating sparse displacement data from iSV involves registering reconstructed cortical surfaces either with respect to pMR at the undeformed state [25, 31] or with each other when acquired at two different surgical stages [26]. Either geometry- or texture intensity-based registrations can be employed because reconstructed stereo surfaces offer both types of information. However, rigid registrations that solely depend on geometry (e.g., iterative closest point, ICP [77]) may not accurately capture surface deformation, especially when significant

lateral shift occurs [26, 78]. In this case, incorporating texture intensity information into the registration will likely improve the accuracy. For example, Paul et al. [26] designed a cost function that includes video image intensity, Euclidean distance between two reconstructed surfaces, and distance between tracked landmarks (i.e., bifurcation locations of major vessels) to derive surface displacements from stereo images captured at two points in time. Results in one patient case demonstrated a significant improvement in registration accuracy compared to the ICP algorithm (2.2 ± 0.2 mm based on a hybrid cost function vs. 5.8 ± 0.9 mm using ICP; the initial alignment was 6.2 ± 2.1 mm). Similarly, Ding et al. [30] used a 3D intensity-encoded point cloud from a laser range scanner to construct 3D surfaces while registering the corresponding 2D image with video images from the microscope to track segmented vessels in order to establish 3D displacement vectors. Results from three patient cases suggested high accuracy in vessel tracking (~ 3 pixels).

More recently, we employed an optical flow motion-tracking algorithm directly on rectified left camera images of a stereo sequence acquired after dural opening. The technique was applied in three patient cases to compute a dense displacement field on the cortical surface from which in-plane surface strain due to blood pressure pulsation was obtained [79]. Because this method does not require landmark localization or vessel segmentation, we anticipate that the same motion-tracking algorithm may also be applicable as a registration technique to derive cortical surface displacements between temporally distinct surgical scenes.

However, these intensity-based registration methods may not be able to register stereo surfaces acquired before and after dural opening because of their substantial dissimilarity in appearance. One approach to solve this problem is to generate a texture map from pMR based on the cortical surface geometry (e.g., either from segmented brain or iSV before dural opening), and then register it with stereo images acquired after dural opening (see Fig. 10 for a typical texture map generated from pMR in comparison with its corresponding stereo image after dural opening).

Common vascular features in both texture maps allow registration using intensity-based algorithms (e.g., via maximization of MI). Because stereovision images are coregistered with pMR (e.g., using fiducial-based patient registration), the two 3D texture maps can be spatially merged to generate their 2D projection images in the same coordinate system, for example, by establishing a local coordinate system with its z -axis parallel to the average nodal normal direction of the texture surface from iSV. The choice of the local coordinate system is important in order to avoid image “folding”. With proper image preprocessing (e.g., Gaussian smoothing; see Fig. 11a), the two images can be registered with an intensity-based rigid algorithm, and 2D displacement vectors can then be obtained (Fig. 11b). Because transformation between the textured cortical surface and its projection image is numerically invertible (e.g., through interpolation), full 3D displacements can be calculated by determining the 3D locations of the starting and ending points of each displacement vector.

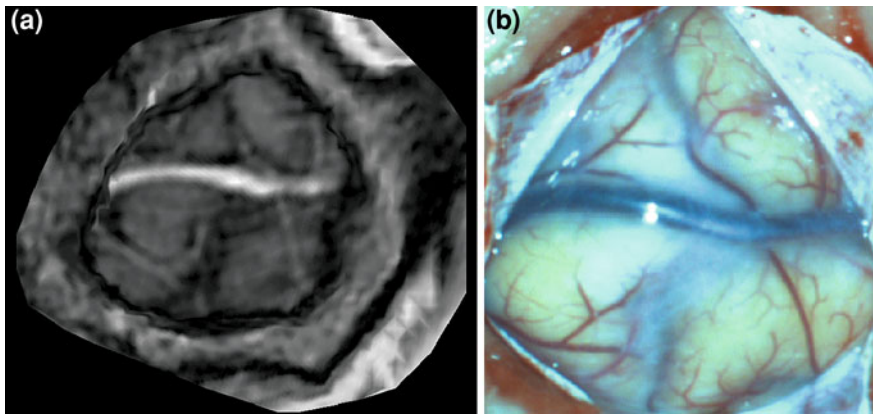


Fig. 10 Comparison between a texture map generated from pMR at the craniotomy (a) and left camera iSV image after dural opening showing corresponding vascular structures (b)

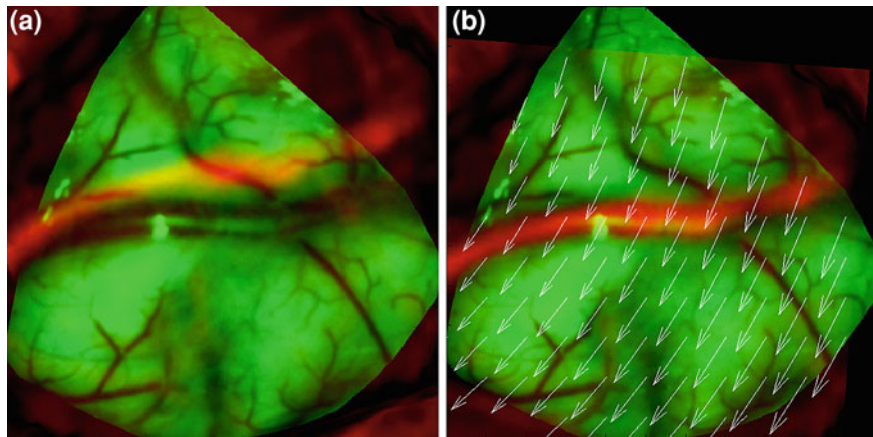


Fig. 11 a Overlay of iSV projection image of the exposed cortical surface (green) and the corresponding textured map from pMR (red; both images Gaussian smoothed); b the same overlay after rigid body registration demonstrating a significant improvement in feature alignment. Sample displacement vectors are also shown (white arrows)

Once registration is completed between the texture map from pMR and the iSV cortical surface obtained after dural opening, iSV cortical surfaces captured at later surgical stages can be used to measure parenchymal surface displacements at any point in time, either relative to the undeformed pMR or the deformed uMR from the previous surgical stage. Consequently, full-volume brain deformation can be estimated using geometries corresponding to either pMR or uMR (at the previous surgical stage) as the reference and evaluating whether the two approaches lead to the same or comparable estimates is of practical importance.

6.4 Modeling of Tumor Resection

Simulation of tumor resection is challenging because no definitive information on the amount or the exact portion of excised tissue is typically available. One approach we have taken produces an initial estimate of the resected tumor tissue and applies a subsequent correction to improve the alignment between uMR and iSV/iUS. Specifically, the surface of the exposed surgical cavity is first reconstructed from iSV and super-imposed on the coregistered FE brain mesh. Brain nodes residing in the surgical cavity (i.e., falling between the new iSV surface and the original, or most recently updated, FE brain mesh surface) are then removed from the mesh to generate a new boundary. The resulting elimination of brain elements is not likely to represent the exact amount of tissue removed because of additional brain movement, for example, from tissue collapse due to release of surface tension once resection begins. To estimate the amount of over- (or possibly under-) removal, subsurface displacement data derived from iUS is assimilated through model inversion on the FE mesh with the newly created iSV surface. If the new model estimates cause brain nodes to cross the iSV surface, their associated elements are removed whereas if voids are created between the FE mesh and the iSV surface, new elements are constructed (so that the FE mesh and new iSV surfaces are coincident). When iUS displacement data is not available, we assume the new iSV surface represents over-removal of tissue and use whole brain deformation resulting from gravitational effects due to loss of buoyancy forces when overlying tissue is removed to estimate the amount of over-removal. In order to correct for over-removal of tissue, the surgical cavity surface reconstructed from iSV is repositioned by an amount opposite to the displacement in the gravitational direction, and only those brain nodes falling outside the repositioned iSV surface are eliminated from the original (or most recently updated) FE mesh.

6.5 Illustration of Model-Estimated Brain Deformation

The goal of estimating intraoperative brain deformation is to generate uMR that incorporates sparse displacements measured intraoperatively in order to allow subsequent neuronavigation. In this sub-section, we illustrate the types of uMR images that can be generated using the techniques presented in this chapter through two clinical cases. The first patient was a 56-year-old male undergoing malignant glioma tumor resection. Both 3D iUS and iSV images were acquired at five temporally distinctive surgical stages (i.e., before and after dural opening, and in the beginning, middle, and at the end of tumor resection). For each surgical stage after dural opening, uMR was generated and compared with iUS and iSV for consistency in parenchymal feature alignment (Fig. 12).

The second patient was a 63-year-old male with recurrent malignant glioma. A pair of iSV images was acquired after the retractor was in place but prior to

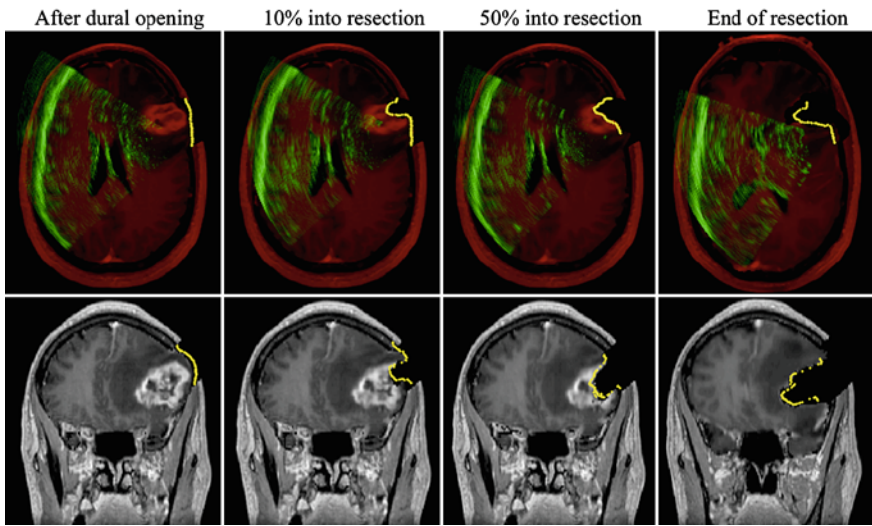
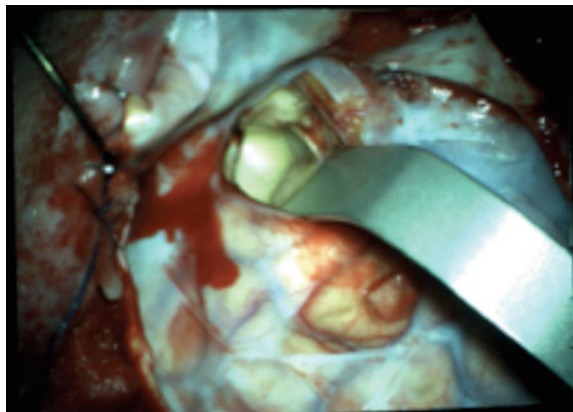


Fig. 12 Representative axial (top) and coronal (bottom) uMR images after dural opening (left), in the beginning ($\sim 10\%$ into resection; second column), middle ($\sim 50\%$ into resection; third column), and at the end of resection (right), overlaid with corresponding cross-sections generated from reconstructed iSV surfaces (yellow line). Axial images are also overlaid with iUS (green). The alignments between iUS, iSV, and uMR with parenchymal features indicate consistency between model estimates and intraoperative measurements

Fig. 13 The left camera iSV image acquired with a retractor in place prior to tumor resection



tissue resection (Fig. 13). The geometrical profiles of the exposed cortical surface and the retractor were then obtained from iSV surface reconstruction, which provided the boundary conditions necessary to deform the brain mesh generated from pMR. The resulting uMR is compared with its pMR counterpart in Fig. 14 along with the corresponding cross-sections of the reconstructed cortical surfaces.

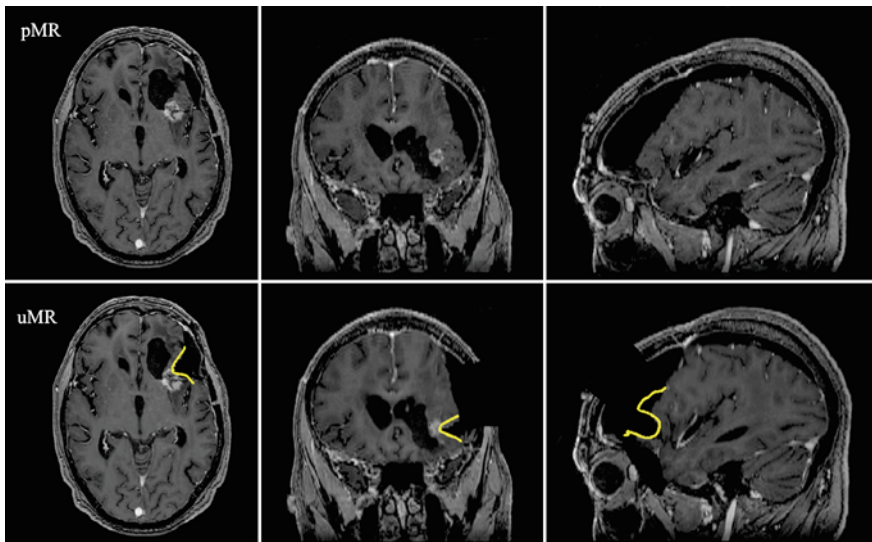


Fig. 14 Comparison of pMR (top) and uMR (bottom) in three orthogonal views after tissue retraction. The corresponding cross-sections of the reconstructed cortical surface are also shown (yellow line). Patient was a 63-old male with recurrent malignant glioma where significant brain shift of the mass was evident before surgery in pMR

These results show that the model-based brain shift compensation strategy is able to generate uMR images resulting from intraoperative brain deformation due to tissue removal (e.g., during tumor resection) and tissue retraction which is important for clinical application of the technique in the OR.

7 Validation of Brain Deformation Estimation

Validation of the computed brain deformation estimates is important for clinical acceptance of model-based brain shift compensation strategies in the OR. Essentially, validation amounts to evaluating the degree of alignment or registration accuracy (ideally in quantitative terms) of homologous features found in the resulting uMR and the coregistered intraoperative images. Therefore, techniques for registration between MR and other imaging modalities such as iMR [35, 43], iSV [25, 31, 47], laser range scanning [28, 30], video images [26, 30], and iUS [21, 69, 80, 81] are applicable. In addition to using tumor margins to measure feature misalignment [69], iUS offers an interesting option based on extracting blood vessels from power Doppler acquisitions to register with their counterparts in MR angiography as a means of evaluating registration accuracy [80, 81]. In this section, we discuss a new validation approach based on tumor tissue fluorescence.

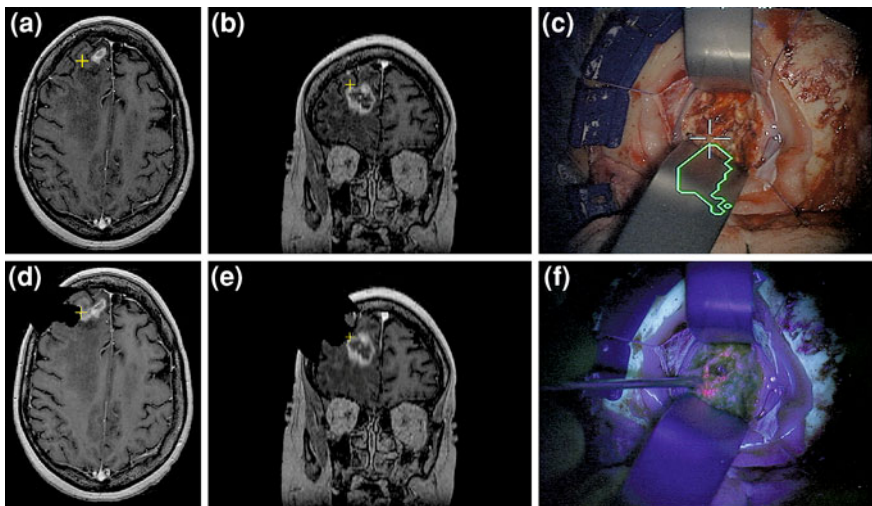


Fig. 15 Comparison of pMR (a, b) and uMR (d, e) in axial and coronal images determined from the microscope focal point (yellow crosses). The focal point was focused on the exposed tumor tissue, the presence of which was evident under blue light conditions (f) but was not evident based on the segmented tumor volume from the coregistered pMR (green contour) under white light conditions (c)

The use of iFI is evolving to be an important surgical aid for maximal tumor resection, especially for certain high-grade glioma tumors. After orally administering δ -aminolevulinic acid (ALA) prior to surgery to enhance endogenous synthesis of the fluorophore protoporphyrin IX (PpIX) in tumor cells, neoplastic tissue with sufficient levels of PpIX will display a red fluorescence when excited under blue light conditions [32, 82, 83]. The resulting fluorescence signature provides a direct visual indication of tumor once it is exposed. iFI can also serve as a means of validating intraoperative brain deformation derived from computational modeling [84] because it provides an independent intraoperative assessment of tumor location.

Figure 15 presents an example of using iFI for validation purposes in a representative patient undergoing tumor resection and tissue retraction. The microscope was focused on the same physical location in the surgical field in which the presence of tumor tissue was evident under blue light fluorescence conditions (Fig. 15f) but was outside the segmented tumor volume in the coregistered pMR shown under white light conditions (Fig. 15c). Because of brain shift, the focal point did not align with tumor in pMR (Fig. 15a, b). However, the alignment was significantly improved when uMR was employed (Fig. 15d, e). These results indicate benefits of a dual-modality approach that combines a deformation model to compensate for intraoperative brain shift with coregistered fluorescence imaging that offers intuitive visual feedback for tumor in the surgical field.

8 Summary and Conclusions

Biomechanical models provide estimates of whole-brain deformation and are important complements to intraoperative imaging techniques for brain shift compensation in image-guided neurosurgery. In this chapter, we have illustrated important aspects of a brain shift compensation strategy based on inverse biomechanical modeling. Specifically, we described the implementation of an inversion scheme to assimilate sparse displacement data, incorporation of brain-skull contact boundary conditions, derivation of sparse displacement data from iUS and iSV, and finally, preliminary results using iFI for validation of the model estimation of intraoperative brain deformation. Because these techniques are designed for implementation in the OR, all of the methods presented are automatic and do not require any manual intervention on the part of the surgeon.

The clinical feasibility of this model-based brain shift compensation strategy depends on its computational efficiency and its clinical utility relies on its updating accuracy. With data guidance, we have shown that an average improvement of 33% in accuracy occurs over the displacement estimates obtained without data guidance in porcine brain retraction, in which approximately 90% of brain deformation was recovered (mean model-data misfit of ~ 1 mm [44]). Using clinical patient cases, we have also demonstrated that tumor displacement estimates degraded (i.e., model-data misfit at the tumor boundary became *worse*) when nodal displacements at the exposed cortical surface were constrained with a forced-displacement method, but improved by 20–43% when these displacements were otherwise assimilated through an inversion method [85]. The accuracy in model estimation can be further improved at the tumor boundary (recovering about 85% of the deformation) as well as at the craniotomy (1.6 mm residual model-data misfit on average) through brain-skull contact BCs because of enhanced model flexibility [47]. These findings suggest that inversion approaches that approximate whole-brain deformation based on locally measured displacement maps are indeed capable of estimating intraoperative brain deformation with sufficient accuracy for clinical applications.

The computational efficiency of the data inversion is significantly improved when using an iterative SGD algorithm instead of the REP approach when the amount of data is large (e.g., $N_{\text{sprs}} > 100$). Although SGD is iterative in nature, employing a direct sparse solver, PARDISO (which utilizes multi-threading), for the per-iteration matrix solutions that are required significantly reduces computation time. Based on five patient cases, an average computational cost of approximately 2 min has been achieved for estimating whole-brain deformation with SGD using 100 sparse data points, and the average initial model-data misfit of 5.2 mm was reduced to 1.1 mm. These results suggest that the SGD algorithm is sufficiently fast with adequate accuracy for routine use in the OR [38].

Because of the data assimilation, inversion performance also depends on the accuracy and computational efficiency of extracting sparse displacement data from iUS and iSV. With 2D iUS, two sequential MI-based re-registrations are necessary

between iUS and pMR before and after dural opening in order to correct for initial image-to-patient registration error and to measure tumor displacement post-durotomy, respectively. Both registrations are automated and the combined computation time is less than 3 min. With volumetric 3D iUS, image rasterization is necessary prior to image registration. A trilinear interpolation algorithm offers improved accuracy and it achieves real-time computational performance comparable to the voxel nearest-neighbor algorithm as well as the fastest pixel-based techniques (1.05 s per full volume with a 1 mm³ voxel size) because it operates in a parametric (instead of the physical) space [75]. To derive sparse displacements from volumetric 3D iUS, one rigid (to correct for misalignment due to errors in tracking/transducer calibration) and one B-Spline nonrigid (to extract feature displacements) registration are necessary. With a set of optimal nonrigid registration parameters (e.g., number of grid nodes along each direction, down-sampling rate, and number of iterations), a computation time of 1–2 min is expected to generate ample sparse displacement vectors (e.g., $N = 100\text{--}200$) for use in data assimilation [86]. In practice, the rigid and nonrigid registrations can be executed simultaneously to further reduce the computation time, in which case feature displacements due to rigid registration can be subtracted from those generated from the nonrigid registration in order to provide data guidance to the model.

The use of iSV and laser range scanning that capture texture-encoded geometrical profiles of the parenchymal surface is emerging as an effective and attractive technique for brain shift compensation. iSV cameras are directly attached to or integrated with the surgical microscope and result in no or minimal intrusion to surgical workflow during image acquisition. Therefore, iSV can be conveniently deployed to capture parenchymal cortical surface at any time during surgery, allowing frequent image updates that would potentially lead to more accurate image-guidance in a typical patient case.

Reports on the accuracy of iSV reconstruction (e.g., ~1 mm [25]) and inter-frame registration between video frames (2 mm [26] or 2–3 pixels [30]) suggest these techniques are sufficiently accurate for clinical applications. However, reports on the computational efficiency of cortical surface displacement extraction are limited at present. Although a processing rate of one-second-per-frame is reported in [30], the computation time related to the semi-automatic vessel segmentation cannot be overlooked [87]. The optical flow motion-tracking algorithm computes a dense displacement field without the need for landmark localization or feature segmentation; however, at the expense of relatively significant computation time (70 s for an image size of 1024 × 768 [79]). Because the computational cost is proportional to the number of pixels, improvements in computational efficiency may be possible by limiting the region of interest to the exposed cortical area via automatic segmentation (instead of using the full size image). In addition, multi-threading or implementation of the algorithm on Graphical Processing Units (GPUs) will likely improve the computational efficiency even further, which will be important to the application of iSV either by itself for brain shift compensation or to provide sparse displacement data for assimilation in an inversion scheme.

Ultimately, validation is necessary to ensure the accuracy of the estimated intraoperative brain deformation. Because iUS and iSV sample the brain independently and are complementary, cross validation of the model estimation with one as the source of intraoperative data for guidance and the other as data for evaluating the accuracy of model solution is possible. In practice, however, both sources of intraoperative displacement data should be utilized in order to maximize estimation accuracy deep in the brain as well as on the cortical surface. In this case, iFI may offer additional verification of the deformation estimates once tumor is exposed. Because fluorescence is currently only available from the tumor surface, model-based image-guidance may play a more important role in the early stages of tumor resection (e.g., before tumor is exposed), while iFI may provide the best form of guidance once tumor is in view. Nevertheless, a model-based, integrated image-guidance approach that incorporates intraoperative imaging techniques is not only important but also possible for routine surgical guidance in the OR.

Acknowledgments Funding from the NIH R01 EB002082-11 and R01 CA159324-01 is acknowledged.

References

1. Lacroix, M., Abi-Said, D., Fourney, D.R., Gokaslan, Z.L., Shi, W., DeMonte, F., Lang, F.F., McCutcheon, I.E., Hassenbusch, S.J., Holland, E., Hess, K., Michael, C., Miller, D., Sawaya, R.: A multivariate analysis of 416 patients with glioblastoma multiforme: prognosis, extent of resection and survival. *J. Neurosurg.* **95**, 190–198 (2001)
2. Laws, E.R., Shaffrey, M.E., Morris, A., Anderson, F.A.: Surgical management of intracranial gliomas—Does radical resection improve outcome? *Acta. Neurochir. Suppl.* **85**, 47–53 (2002)
3. Buckner, J.C.: Factors influencing survival in high-grade gliomas. *Semin. Oncol.* **30**, 10–14 (2003)
4. Pichlmeier, U., Bink, A., Schackert, G., Stummer, W.: Resection and survival in glioblastoma multiforme: an RTOG recursive partitioning analysis of ALA study patients. *Neuro. Oncol.* **10**, 1025–1034 (2008)
5. Stummer, W., Reulen, H.J., Meinel, T., Pichlmeier, U., Schumacher, W., Tonn, J.C., et al.: Extent of resection and survival in glioblastoma multiforme: identification of and adjustment for bias. *Neurosurgery* **62**, 564–576 (2008)
6. Maurer, C.R., Fitzpatrick, J.M., Wang, M.Y., Galloway, R.L., Maciunas, R.J., Allen, G.S.: Registration of head volume images using implantable fiducial markers. *IEEE Tran. Med. Imag.* **16**(4), 447–462 (1997)
7. West, J., et al.: Comparison and evaluation of retrospective intermodality brain image registration techniques. *J. Comput. Assist. Tomogr.* **21**(4), 554–566 (1997)
8. Helm, P.A., Eckel, T.S.: Accuracy of registration methods in frameless stereotaxis. *Comput. Aided Surg.* **3**, 51–56 (1998)
9. Ammirati, M., Gross, J.D., Ammirati, G., Dugan, S.: Comparison of registration accuracy of skin-and bone-implanted fiducials for frameless stereotaxis of the brain: a prospective study. *Skull Base.* **12**(3), 125–130 (2002)

10. Hill, D.L.G., Maurer, C.R., Maciunas, R.J., Barwise, J.A., Fitzpatrick, J.M., Wang, M.Y.: Measurement of intraoperative brain surface deformation under a craniotomy. *Neurosurgery* **43**(3), 514–526 (1998)
11. Roberts, D.W., Hartov, A., Kennedy, F.E., Miga, M.I., Paulsen, K.D.: Intraoperative brain shift and deformation: a quantitative analysis of cortical displacement in 28 cases. *Neurosurgery* **43**(4), 749–760 (1998)
12. Nimsky, C., Ganslandt, O., Cerny, S., Hasteiter, P., Greiner, G., Falbusch, R.: Quantification of, visualization of and compensation for brain shift using intraoperative magnetic resonance imaging. *Neurosurgery* **47**(5), 1070–1080 (2000)
13. Nabavi, A., Black, P.M., Gering, D.T., Westin, C.F., Mehta, V., Pergolizzi Jr, R.S., Ferrant, M., Warfield, S.K., Hata, N., Schwartz, R.B., Wells III, W.M., Kikinis, R., Jolesz, F.A.: Serial intraoperative magnetic resonance imaging of brain shift. *Neurosurgery* **48**(4), 787–798 (2001)
14. Hartkens, T., Hill, D.L.G., Castellano-Smith, A.D., Hawkes Jr, D.J., Maurer, C.R., Martin, M.J., Hall, W.A., Liu, H., Truwit, C.L.: Measurement and analysis of brain deformation during neurosurgery. *IEEE Trans. Med. Imaging* **22**(1), 82–92 (2003)
15. Ferrant, M., Nabavi, A., Macq, B., Black, P.M., Jolesz, F.A., Kinkinis, R., Warfield, S.K.: Serial registration of intraoperative MR images of the brain. *Med. Image Anal.* **6**, 337–359 (2002)
16. Hall, W.A., Liu, H., Martin, A.J., Pozza, C.H., Maxwell, R.E., Truwit, C.L.: Safety, efficacy, and functionality of high-field strength interventional magnetic resonance imaging for neurosurgery. *Neurosurgery* **46**, 632–642 (2000)
17. Nimsky, C., Ganslandt, O., Hasteiter, P., Fahrbush, R.: Intraoperative compensation for brain shift. *Surg. Neurol.* **56**, 357–365 (2001)
18. Wirtz, C.R., Bonsanto, M.M., Knauth, M., Tronnier, V.M., Albert, F.K., Staubert, A., Kunze, S.: Intraoperative magnetic resonance imaging to update interactive navigation in neurosurgery: method and preliminary experience. *Comput. Aided Surg.* **2**, 172–179 (1997)
19. Bonsanto, M.M., Staubert, A., Wirtz, C.R., Tronnier, V., Kunze, S.: Initial experience with an ultrasound-integrated single-rack neuronavigation system. *Acta Neurochir.* **143**(11), 1127–1132 (2001)
20. Bucholz, R.D., Smith, K.R., Laycock, K.A., McDermont, L.L.: Three-dimensional localization: from image-guided surgery to information-guided therapy. *Methods (Duluth)* **25**(2), 186–200 (2001)
21. Comeau, R.M., Sadikot, A.F., Fenster, A., Peters, T.M.: Intraoperative ultrasound for guidance and tissue shift correction in image-guided neurosurgery. *Med. Phys.* **27**, 787–800 (2000)
22. Rasmussen Jr, I.A., Lindseth, F., Rygh, O.M., Berntsen, E.M., Selbekk, T., Xu, J., Nagelhus Hernes, T.A., Harg, E., Häberg, A., Unsgaard, G.: Functional neuronavigation combined with intra-operative 3D ultrasound: initial experiences during surgical resections close to eloquent brain areas and future directions in automatic brain shift compensation of preoperative data. *Acta Neurochir. (Wien)* **149**(4), 365–378 (2007)
23. Ji, S., Fontaine, K., Hartov, A., Borsic, A., Roberts, D.W., Paulsen, K.D.: Coregistered volumetric true 3D ultrasonography in image-guided neurosurgery. In: Miga, M.I., Cleary, K.R. (eds.) *Medical Imaging 2008: Visualization, Image-Guided Procedures, and Modeling*. Proceedings of SPIE. vol. 6918. SPIE, Bellingham, 2008, 69180F
24. Skrinjar, O., Nabavi, A., Duncan, J.: Model-driven brain shift compensation. *Med. Image Anal.* **6**(4), 361–373 (2002)
25. Sun, H., Lunn, K.E., Farid, H., Wu, Z., Roberts, D.W., Hartov, A., Paulsen, K.D.: Stereopsis-guided brain shift compensation. *IEEE Trans. Med. Imag.* **24**(8), 1039–1052 (2005)
26. Paul, P., Morandi, X., Jannin, P.: A surface registration method for quantification of intraoperative brain deformations in image-guided neurosurgery. *IEEE Trans. Info. Tech. Biomed.* **13**(6), 976–983 (2009)

27. DeLorenzo, C., Papademetris, X., Staib, L.H., Vives, K.P., Spencer, D.D., Duncan, J.S.: Image-guided intraoperative cortical deformation recovery using game theory: application to neocortical epilepsy surgery. *IEEE Trans. Med. Imag.* **29**(2), 322–338 (2010)
28. Miga, M.I., Sinha, T.K., Cash, D.M., Galloway, R.L., Weil, R.J.: Cortical surface registration for image-guided neurosurgery using laser-range scanning. *IEEE Trans. Med. Imag.* **22**(8), 973–985 (2003)
29. Cao, A., Thompson, R.C., Dumpuri, P., Dawant, B.M., Galloway, R.L., Ding, S., Miga, M.I.: Laser range scanning for image-guided neurosurgery: investigation of image-to-physical space registrations. *Med. Phys.* **35**(4), 1593–1605 (2008)
30. Ding, S., Miga, M.I., Pheiffer, T.S., Simpson, A.L., Thompson, R.C., Dawant, B.M.: Tracking of vessels in intra-operative microscope video sequences for cortical displacement estimation. *IEEE Trans. Biomed. Eng.* **58**(7), 1985–1993 (2011)
31. DeLorenzo, C., Papademetris, X., Wu, K., Vives, K.P., Spencer, D., Duncan, J.S.: Nonrigid 3D brain registration using intensity/feature information. *Lecture Notes in Computer Science*, vol. 4190, pp. 932–939. Springer, Berlin (2006)
32. Stummer, W., Stocker, S., Wagner, S., Stepp, H., Fritsch, C., Goetz, C., Goetz, A.E., Kieffmann, R., Reulen, H.J.: Intraoperative detection of malignant gliomas by 5-aminolevulinic acid-induced porphyrin fluorescence. *Neurosurgery* **42**, 518–525 (1998). Discussion pp. 525–516
33. Lin, W.C., Toms, S.A., Motamedi, M., Jansen, E.D., Mahadevan-Jansen, A.: Brain tumor demarcation using optical spectroscopy: an in vitro study. *J. Biomed. Opt.* **5**, 214–220 (2000)
34. Valdes, P.A., Leblond, F., Anthon, Y.K., Harris, B.T., Wilson, B., Fan, X., Tosteson, T.D., Hartov, A., Ji, S., Erkmen, K., Simmons, N.E., Paulsen, K.D., Roberts, D.W.: Quantitative fluorescence in intracranial tumor: implications for ALA-induced PpIX as an intraoperative biomarker. *J. Neurosurg.* **115**, 11–17 (2011)
35. Hu, J., Jin, X., Lee, J.B., Zhang, L., Chaudhary, V., Guthikonda, M., Yang, K.H., King, A.I.: Intraoperative brain shift prediction using a 3D inhomogeneous patient-specific finite element model. *J. Neurosurg.* **106**, 164–169 (2007)
36. Wittek, A., Kikinis, R., Warfield, S.K., Miller, K.: Brain shift computation using a fully nonlinear biomechanical model. *Med. Image. Comput. Comput. Assist. Inter.* **8**(Pt 2), 583–590 (2005)
37. Lunn, K.E., Paulsen, K.D., Lynch, D.R., Roberts, D.W., Kennedy, F.E., Hartov, A.: Assimilating intraoperative data with brain shift modeling using the adjoint equations. *Med. Image Anal.* **9**, 281–293 (2005)
38. Ji, S., Hartov, A., Roberts, D.W., Paulsen, K.D.: Data assimilation using a gradient descent method for estimation of intraoperative brain deformation. *Med. Image Anal.* **13**(5), 744–756 (2009)
39. Miller, K., Wittek, A., Joldes, G.: Biomechanics of the brain for computer-integrated surgery. *Acta Bioeng. Biomech.* **12**(2), 25–37 (2010)
40. Dumpuri, P., Thompson, R.C., Dawant, B.M., Cao, A., Miga, M.I.: An atlas-based method to compensate for brain shift: preliminary results. *Med. Image Anal.* **11**(2), 128–145 (2007)
41. Dumpuri, P., Thompson, R.C., Cao, A., Ding, S., Garg, I., Dawant, B.M., Miga, M.I.: A fast efficient method to compensate for brain shift for tumor resection therapies measured between preoperative and postoperative tomograms. *IEEE Trans. Biomed. Eng.* **57**(6), 1285–1296 (2010)
42. Chen, I., Coffey, A.M., Ding, S., Dumpuri, P., Dawant, B.M., Thompson, R.C., Miga, M.I.: Intraoperative brain shift compensation: accounting for dural septa. *IEEE Trans. Biomed. Eng.* **58**(3), 499–508 (2011)
43. Clatz, O., Delingette, H., Talos, I.F., Golby, A.J., Kikinis, R., Jolesz, F.A., Ayache, N., Warfield, S.K.: Robust nonrigid registration to capture brain shift from intraoperative MRI. *IEEE Trans. Med. Imaging* **24**(11), 1417–1427 (2005)

44. Lunn, K.E., Paulsen, K.D., Liu, F., Kennedy, F.E., Hartov, A., Roberts, D.W.: Data-guided brain deformation modeling: evaluation of a 3-D adjoint inversion method in porcine studies. *IEEE Trans. Biomed. Eng.* **53**(10), 1893–1900 (2006)
45. Sun, H., Lunn, K.E., Faird, H., Wu, Z., Roberts, D.W., Hartov, A., Paulsen, K.D.: Stereopsis-guided brain shift compensation. *IEEE Trans. Med. Imaging* **24**(8), 1039–1052 (2005)
46. DeLorenzo, C., Papademetris, X., Vives, K.P., Spencer, D.D., Duncan, J.S.: A comprehensive system for intraoperative 3D brain deformation recovery. *MICCAI Part II, LNCS* 4792 (2007), pp. 553–561
47. Ji, S., Roberts, D.W., Hartov, A., Paulsen, K.D.: Brain-skull contact boundary condition in an inverse computational model. *Med. Image Anal.* **13**(4), 659–672 (2009)
48. Carter, T.J., Sermesant, M., Cash, D.M., Barratt, D.C., Tanner, C., Hawkes, D.J.: Application of soft tissue modeling to image-guided surgery. *Med. Eng. Phys.* **27**, 893–909 (2005)
49. Kobashi, K., Papademetris, X., Duncan, J.S.: A new biomechanical model based approach on brain shift compensation. In: Ellis, R.E., Peters, T.M. (eds.) *MICCAI, LNCS* 2878 (2003), pp. 59–66
50. Biot, M.: General theory of three-dimensional consolidation. *J. Appl. Phys.* **12**, 155–164 (1941)
51. Bilston, L.E., Zizhen, L.: Phan-Tien Nhah: linear viscoelastic properties of bovine brain tissue in shear. *Biorheology* **34**(6), 377–385 (1997)
52. Zhang, L., Yang, K.H., King, A.I.: A proposed injury threshold for mild traumatic brain injury. *J. Biomech. Eng.* **126**, 226–236 (2004)
53. Mendis, K.K., Stalnaker, R.L., Advani, S.H.: A constitutive relationship for large deformation finite element modeling of brain tissue. *J. Biomech. Eng.* **117**, 279–285 (1995)
54. Miller, K., Chinzei, K., Orssengo, G., Bednarz, P.: Mechanical properties of brain tissue in vivo: experiment and computer simulation. *J. Biomech.* **33**(11), 1369–1376 (2000)
55. Kleiven, S., Hardy, W.N.: Correlation of an FE model of the human head with local brain motion—consequences for injury prediction. *Stapp Car Crash J.* **46**, 123–144 (2002)
56. Paulsen, K.D., Miga, M.I., Kennedy, F.E., Hoopes, P.J., Hartov, A., Roberts, D.W.: A computational model for tracking subsurface tissue deformation during stereotactic neurosurgery. *IEEE Trans. Biomed. Eng.* **46**, 213–225 (1999)
57. Miga, M.I.: Development and quantification of a 3D brain deformation model for model-updated image-guided stereotactic neurosurgery. Dartmouth College, Thayer School of Engineering, Hanover. (1998)
58. Platenik, L.A., Miga, M.I., Roberts, D.W., Lunn, K.E., Kennedy, F.E., Hartov, A., Paulsen, K.D.: In vivo quantification of retraction deformation modeling for updated image-guidance during neurosurgery. *IEEE Trans. Biomed. Eng.* **49**(8), 823–835 (2002)
59. Ghadyani, H., Sullivan, J., Wu, Z.: Boundary recovery for delaunay tetrahedral meshes using local topological transformations. *Finite Elem. Anal. Des.* **46**(1–2), 74–83 (2010)
60. Ji, S., Ford, J.C., Greenwald, R.M., Beckwith, J.G., Paulsen, K.D., Flashman, L.A., McAllister, T.W.: Automated subject-specific, hexahedral mesh generation via image registration. *Finite Elem. Anal. Des.* **47**, 1178–1185 (2001)
61. Lynch, D.: Numerical Partial Differential Equations for Environmental Scientists and Engineers. Springer, Berlin (2004)
62. Schenk, O., Gartner, K.: Solving unsymmetric sparse systems of linear equations with PARDISO. *J. Future Gen. Compu. Syst.* **20**(3), 475–487 (2004)
63. Gould, N.I.M., Scott, J.A., Hu, Y.: A numerical evaluation of sparse direct solvers for the solution of large sparse symmetric linear systems of equations. *ACM Trans. Math. Softw.*, **33**(2) Article 10:1–10:32 (2007)
64. Bramley, R., Wang, X.: SPLIB: a library of iterative methods for sparse linear systems, Department of Computer Science, Indiana University, Bloomington, (1997) <http://www.cs.indiana.edu/ftp/bramley/splib.tar.gz>
65. Ji, S., Liu, F., Hartov, A., Roberts, D.W., Paulsen, K.D.: Brain-skull boundary conditions in a neurosurgery deformation model. In: Miga M.I., Cleary K.R. (eds.) *Medical Imaging 2007:*

- Visualization and Image-Guided Procedures. Proceedings of SPIE, vol. 6509. (SPIE, Bellingham 2007), 65092J
- 66. Laursen, T.A.: Computational contact and impact mechanics: fundamentals of modeling interfacial phenomena in nonlinear finite element analysis. Springer-Verlag, Berlin (2002)
 - 67. Zhong, Z.H.: Finite element procedures for contact-impact problems. Oxford Science Publications, London (1993)
 - 68. Le Tallec, P.: Numerical methods for solids. In: Ciarlet, P.G., Lions, J.L. (eds.) *Handbook of numerical analysis*. North-Holland, Amsterdam (1994)
 - 69. Ji, S., Wu, Z., Hartov, A., Roberts, D.W., Paulsen, K.D.: Mutual-information-based patient registration using intraoperative ultrasound in image-guided neurosurgery. *Med. Phys.* **35**(10), 4612–4624 (2008)
 - 70. Fenster, A., Downey, D.B., Cardinal, H.N.: Three-dimensional ultrasound imaging. *Phy. Med. Bio.* **46**, R67–R99 (2001)
 - 71. Unsgaard, A., Rygh, O.M., Selbekk, T., Buller, T.B., Kolstad, F., Lindseth, F., Nagelhus Hernes, T.A.: Intraoperative 3D ultrasound in neurosurgery. *Acta Neurochir.* **148**, 235–253 (2006)
 - 72. Rohling, R., Gee, A., Berman, L.: A comparison of freehand three-dimensional ultrasound reconstruction techniques. *Med. Image Anal.* **3**, 339–359 (1999)
 - 73. Solberg, O.V., Lindseth, F., Torp, H., Blake, R.E., Nagelhus Hernes, T.A.: Free-hand 3D ultrasound reconstruction algorithms: a review. *Ultrasound Med. Biol.* **33**, 991–1009 (2007)
 - 74. Hartov, A., Paulsen, K.D., Ji, S., Fontaine, K., Furun, M., Borsic, A., Roberts, D.W.: Adaptive spatial calibration of a 3D ultrasound system. *Med. Phys.* **37**(5), 2121–2130 (2010)
 - 75. Ji, S., Roberts, D.W., Hartov, A., Paulsen, K.D.: Real-time interpolation for true 3-dimensional ultrasound image volumes. *J. Ultrasound Med.* **30**, 241–250 (2011)
 - 76. Ji, S., Roberts, D.W., Hartov, A., Paulsen, K.D.: Combining multiple volumetric true 3D ultrasound volumes through re-registration and rasterization. In: Yang, G.-Z. et al. (eds.) MICCAI Part I, LNCS 5761 (2009). pp. 795–802
 - 77. Besl, P.J., McKay, N.D.: A method for registration of 3-d shapes. *IEEE. Trans. Pattern. Anal. Mach. Intell.* **14**(2), 239–256 (1992)
 - 78. Fan, X., Ji, S., Hartov, A., Roberts, D., Paulsen, K.: Registering stereovision surface with preoperative magnetic resonance images for brain shift compensation. In: David, R., Holmes, III., Kenneth, H. Wong. (eds.) Medical Imaging 2012: Image-Guided Procedures, Robotic Interventions, and Modeling, Proceedings of SPIE vol. 8316. (SPIE, Bellingham 2012), 83161C
 - 79. Ji, S., Fan, X., Roberts, D.W., Paulsen, K.D.: Cortical surface strain estimation using stereovision. In: Fichtinger, G., Martel, A., Peters, T. (eds.) MICCAI, Part I, LNCS 6891 (2011). pp. 412–419
 - 80. Reinertsen, I., Lindseth, F., Unsgaard, G., Collins, D.: Clinical validation of vessel-based registration for correction of brain-shift. *Med. Image Anal.* **11**(6), 673–684 (2007)
 - 81. Slomka, P.J., Mandel, J., Downey, D., Fenster, A.: Evaluation of voxel-based registration of 3-D power Doppler ultrasound and 3-D magnetic resonance angiographic images of carotid arteries. *Ultrasound Med. Biol.* **27**(7), 945–955 (2001)
 - 82. Stummer, W., Stepp, H., Moller, G., Ehrhardt, A., Leonhard, M., Reulen, H.J.: Technical principles for protoporphyrin-IX-fluorescence guided microsurgical resection of malignant glioma tissue. *Acta Neurochir. (Wien)* **140**, 995–1000 (1998)
 - 83. Stummer, W., Reulen, H.J., Novotny, A., Stepp, H., Tonn, J.C.: Fluorescence-guided resections of malignant gliomas—an overview. *Acta Neurochir. Suppl.* **88**, 9–12 (2003)
 - 84. Valdes, P.A., Fan, X., Ji, S., Harris, B.T., Paulsen, K.D., Roberts, D.W.: Estimation of brain deformation for volumetric image updating in protoporphyrin IX fluorescence-guided resection. *Stereotact. Funct. Neurosurg.* **88**, 1–10 (2010)
 - 85. Liu, F., Paulsen, K.D., Lunn, K., Sun, H., Hartov, A., Wu, Z., Roberts, D.W.: Comparative study of brain deformation estimation methods. In: Cleary, K.R., Galloway, R.L. Jr. (eds.) Medical Imaging 2006: Visualization, Image-Guided Procedures, and Display, Proceedings of SPIE. vol. 6141. (SPIE, Bellingham 2006), 61411D

86. Ji, S., Fan, X., Roberts, D.W., Hartov, A., Paulsen, K.D.: Optimizing nonrigid registration performance between volumetric true 3D ultrasound images in image-guided neurosurgery. In: Medical Imaging 2011: Visualization, Display and Image-Guided Procedures. Proceedings of SPIE, Lake Buena Vista (2011)
87. Ding, S., Miga, M.I., Noble, J.H., Cao, A., Dompuri, P., Thompson, R.C., Dawant, B.M.: Semiautomatic registration of pre- and post brain tumor resection laser range data: method and validation. *IEEE Trans. Biomed. Eng.* **56**(3), 770–780 (2009)